nature communications

Article

https://doi.org/10.1038/s41467-026-74707-4

Fibronectin-induced overactivation of $\alpha_V\beta_3$-PI3K-PIP3-PDK1-ILK signaling drives aortic disease in Marfan syndrome

Received: 18 November 2024

Accepted: 12 June 2026

Published online: 06 July 2026

Check for updates

Iván Alarcón-Ruiz[1,2], María Jesús Ruiz-Rodríguez[1,2,11,14], Sara Martínez-Martínez[1,2,14], Marta Toral[1,2,12,14], Noelia Martín-Bermejo[1,2], Sergio Mateos-García[1,2], Teresa Gil-Ruiz[3], Elías Herrero-Galán[4], María José Méndez-Olivares[1,2], Dolores López-Maderuelo[1,2,13], Carolina Gutiérrez-Martínez[3], Cristina Clemente[3], Alejandro Clemente-Manteca[4], Alberto H-Alcántara[3], Andrea Guala[2,5], Arturo Evangelista[6], Gisela Teixido-Tura[2,5], Diego Rodríguez-Puyol[7], Juan Francisco Nistal[2,8], Jorge Alegre-Cebollada[2,4], Jesús Vázquez[2,9], Juan Duarte[2,10], Juan Miguel Redondo[1,2,3,15] ✉ & Miguel R. Campanero[2,3,15] ✉

Thoracic aortic aneurysms and dissections (TAAD), a life-threatening complication of Marfan syndrome (MFS), lack curative therapies. Our previous studies revealed that versican accumulation drives MFS aortopathy through AKT-NO pathway overactivation, but the upstream mechanisms remained unclear. Here, we show that versican-driven fibronectin (FN) accumulation activates an $\alpha_V\beta_3$-PI3K-PIP3-PDK1-ILK signaling cascade leading to AKT-NOS2 upregulation and aortic disease. FN accumulates in aortas of MFS patients and mice of both sexes and correlates with increased $\alpha_V\beta_3$ integrin and ILK expression. Disrupting FN assembly or inhibiting $\alpha_V\beta_3$, PI3K, PIP3, PDK1 or ILK prevents FN-induced AKT activation and NOS2 upregulation, restores vascular contractility, and limits aortic dilation in MFS mice. Inhibition of ILK or PDK1, aortic silencing of *Ilk*, or smooth muscle-specific deletion of *Ilk* reverses or prevents aortic growth. Together, these findings define a mechanistically integrated FN-$\alpha_V\beta_3$-PI3K-PIP3-PDK1-ILK-AKT-NOS2 signaling cascade in MFS and support its causative role in human TAAD, highlighting its components as potential targets for therapeutic intervention.

Aortic aneurysm (AA) is a clinically stealthy disorder characterized by the progressive enlargement of the aorta, which can lead to aortic dissection, posing a high mortality risk. Aortic dissections account for 1–2% of all deaths in industrialized countries[1,2]. However, they are frequently misdiagnosed as myocardial infarctions, and this figure may underestimate their true deadly potential[3]. AAs are classified based on their location into abdominal aortic aneurysms and thoracic aortic aneurysms (TAAs). Approximately 25% of TAADs have an identifiable genetic basis, with at least 35 genes associated to date[4]. Mutations in these genes lead to extracellular matrix (ECM) remodeling, vascular smooth muscle cells (VSMCs) dysfunction, and disruption of the TFG-β signaling pathway[4].

TAADs with a genetic basis are associated with both syndromic entities such as Marfan syndrome (MFS) and non-syndromic diseases. MFS, inherited in an autosomal dominant manner, results from mutations in the *FBN1* gene, encoding the ECM glycoprotein fibrillin-1[5]. This disorder manifests as multisystemic connective tissue abnormalities, resulting in skeletal, ocular, skin, and cardiovascular

A full list of affiliations appears at the end of the paper. ✉e-mail: jmredondo@cbm.csic.es; mcampanero@cbm.csic.es

complications, with TAAD contributing to >90% of MFS-related fatalities[6–8]. Current MFS management involves close monitoring, lifestyle adjustments, medical treatments to decelerate aortic growth, and prophylactic surgery targeting affected aortic segments, all aimed at preventing dissection and premature mortality[9]. Pharmacological therapy typically relies on β-adrenoreceptor blockade and angiotensin receptor blockers[9]. However, these treatments have limited efficacy in preventing aortic dissection and mortality, and some studies even suggest that β-adrenergic blockers may not slow aortic growth in MFS, leaving surgery as the sole effective prophylactic intervention[10–12]. There is therefore an urgent need for effective pharmacological strategies to manage TAADs in MFS patients, which would greatly benefit from a deeper understanding of the molecular mechanisms underlying TAA formation.

Accumulation of proteoglycans in the aortic wall is a hallmark of TAA, and our recent research has revealed that accumulation of the versican (VCAN) proteoglycan leads to increased expression of the inducible nitric oxide synthase (iNOS or NOS2) and aortopathy in MFS[13]. This finding aligns with observations indicating that downregulation of ADAMTS1, a metalloproteinase cleaving versican, leads to NOS2 induction, and pharmacological inhibition of NOS2 reverses aortic dilation in the *Fbn1*$^{C1041G/+}$ mouse model of MFS[14]. Notably, NOS2-mediated nitric oxide (NO) overproduction elicits protein kinase G (PKG) overactivation[15], potentially inhibiting the contractile capacity of VSMCs. The elastin-contractile unit, the connection of the contractile apparatus of VSMCs to elastic fibers, is essential for mechanosensing and force transmission from the ECM to muscle cells and vice versa, ultimately maintaining the integrity of the aortic wall[16,17]. Fibrillin-1 microfibrils provide a scaffold for elastic fiber formation and maturation[18]. As MFS-related *FBN1* mutations impair fibrillin microfibrils formation and stability, they hinder elastic fiber formation, thus disrupting the elastin-contractile unit, compromising aortic wall integrity, and leading to TAA[18]. Similarly, genetic mutations in other components of the elastin-contractile unit result in TAAD[17]. Collectively, these findings strongly support the notion that dysregulation of the contractile capacity of the aorta may predispose to TAAD.

Here, we show that VCAN contributes to the accumulation of fibronectin (FN), an ECM component that builds up in the wall of MFS aortas. FN induces NOS2 expression, impairs aortic contractility, and promotes aortopathy in MFS through integrin $\alpha_V\beta_3$-mediated signaling involving PI3K, PIP3, PDK1, and ILK. Indeed, structural FN disruption, as well as genetic knockdown (KD), knockout (KO), or pharmacological inhibition of essential components of this signaling pathway effectively reversed MFS-associated aortic disease.

Results

Fibronectin accumulation in the aorta drives aortic dilation in MFS

To uncover potential mediators underlying MFS aortopathy, we conducted a high-throughput proteomic analysis of aortas from wild-type (WT) and *Fbn1*$^{C1041G/+}$ mice. Twelve-week-old animals were intentionally selected to enrich for early pathogenic pathways while minimizing secondary changes associated with advanced aortic wall degeneration, thereby facilitating the identification of disease-initiating mechanisms. While fibrillin-1 exhibited the most significant downregulation in this model, FN was the most significantly upregulated protein (Fig. 1a). Quantitative PCR analysis of aortic extracts revealed increased *Fn1* mRNA in MFS mice (Fig. 1b), and immunofluorescence staining of aortic sections also revealed increased FN levels in both male and female MFS mice (Fig. 1c, d). Remarkably, FN accumulation was also evident in the aortic medial layer of MFS patients compared to control aortas obtained from organ transplant donors (Fig. 1e and Supplementary Fig. 1).

Given our previous findings that VCAN accumulation induces NOS2 expression and drives aortopathy in MFS, and that lentivirus-mediated *Vcan* knockdown reverses this phenotype[13], we employed archived aortic samples from that study to investigate the potential cross-talking between FN and VCAN accumulation to promote NOS2 activation and aortic disease. Strikingly, immunostaining of aortic sections from MFS mice subjected to *Vcan* knockdown revealed that the reversal of aortopathy observed in that study[13] was accompanied by a marked reduction in FN levels in the medial layer, restoring them to WT levels (Fig. 1f, g).

It is important to note that FN is secreted as inactive dimers and that its biological activity depends on its assembly into multimeric fibrillar structures[19,20]. To investigate the contribution of FN to MFS aortopathy, we employed a peptide containing FUD, an adhesin-derived peptide that binds the FN assembly domain and disrupts FN-FN interactions, thereby preventing FN activation[21,22]. FUD was fused to a 6x-His tag to enable tissue detection. In primary VSMC cultures, FUD treatment markedly inhibited FN matrix deposition (Supplementary Fig. 2a). Moreover, when applied after 2 days of culture, FUD efficiently disrupted pre-assembled FN matrix (Supplementary Fig. 2b).

To evaluate FN-dependent cell adhesion, CFSE-labeled VSMCs were seeded onto plates coated with BSA (control), FN, or FN plus FUD. VSMCs adhered to FN-coated surfaces, but this adhesion was abolished in the presence of FUD (Supplementary Fig. 2c). Together, these findings demonstrate that FUD effectively prevents and dismantles FN assembly, thereby abrogating FN-dependent cell adhesion.

To assess the effect of FN assembly inhibition in MFS mice, animals received daily intraperitoneal FUD injections for 1 week. Aortic dimensions were monitored by ultrasound before treatment and on days 2, 4 and 6; mice were euthanized on day 7, and the aorta was harvested for immunofluorescence analysis (Fig. 1h). FUD treatment normalized the diameter of the ascending aorta (AsAo) within 4 days and markedly reduced the diameter of the aortic root (AoRoot) and the abdominal aorta (AbAo) in MFS mice (Fig. 1i, j). Immunofluorescence staining of the 6x-His tag in aortic sections confirmed the presence of FUD in the aortic medial layer, without altering overall Fn or Vcan levels (Supplementary Figs. 3a–c).

To determine the functional consequences of FN disruption on ECM organization, we analyzed collagen type I deposition, which depends on FN fibrils for proper assembly[23]. Immunostaining revealed reduced collagen-I levels in the aortic media of FUD-treated MFS mice (Supplementary Fig. 3d). Since FN interaction with fibrillin-1 within elastic fibers requires FN multimerization[24], we hypothesized that FN disruption by FUD would alter ECM-elastic fibers interaction. Second Harmonic Generation (SHG) microscopy revealed organized ECM deposition around elastic fibers in WT and untreated MFS mice, whereas ECM was substantially dissociated from the elastic fibers in FUD-treated MFS mice (Supplementary Fig. 4a). Consistently, FN signal in regions proximal to elastin (<2.5 μm from elastic fibers) was significantly reduced following FUD treatment (Supplementary Fig. 4b). Given that ECM remodeling affects tissue stiffness and cellular behavior[25], we next assessed aortic stiffness using Atomic Force Microscopy (AFM). MFS aortas were stiffer than WT, but overnight incubation with FUD normalized stiffness values (Supplementary Fig. 4c). Collectively, these findings demonstrate that FUD prevents and dismantles FN assembly, inhibits FN-mediated cell adhesion, and restores normal mechanical properties in MFS aortas.

Fibronectin impairs aortic contractility

Our previous studies underscored the causal role of Nos2 overexpression, NO overproduction, and Pkg overactivation in the development of MFS-related aortopathy[2,14,15]. To investigate whether FN mediates its effects in the aorta through this signaling pathway, we evaluated the impact of FUD administration on the expression of Nos2 and, as a readout of Pkg activation, the phosphorylation of its substrate Vasp at S239 (pVasp^{S239})[15]. Immunostaining of AsAo sections revealed that FUD reversed Nos2 induction and Pkg overactivation, as

https://doi.org/10.1038/s41467-026-74707-4

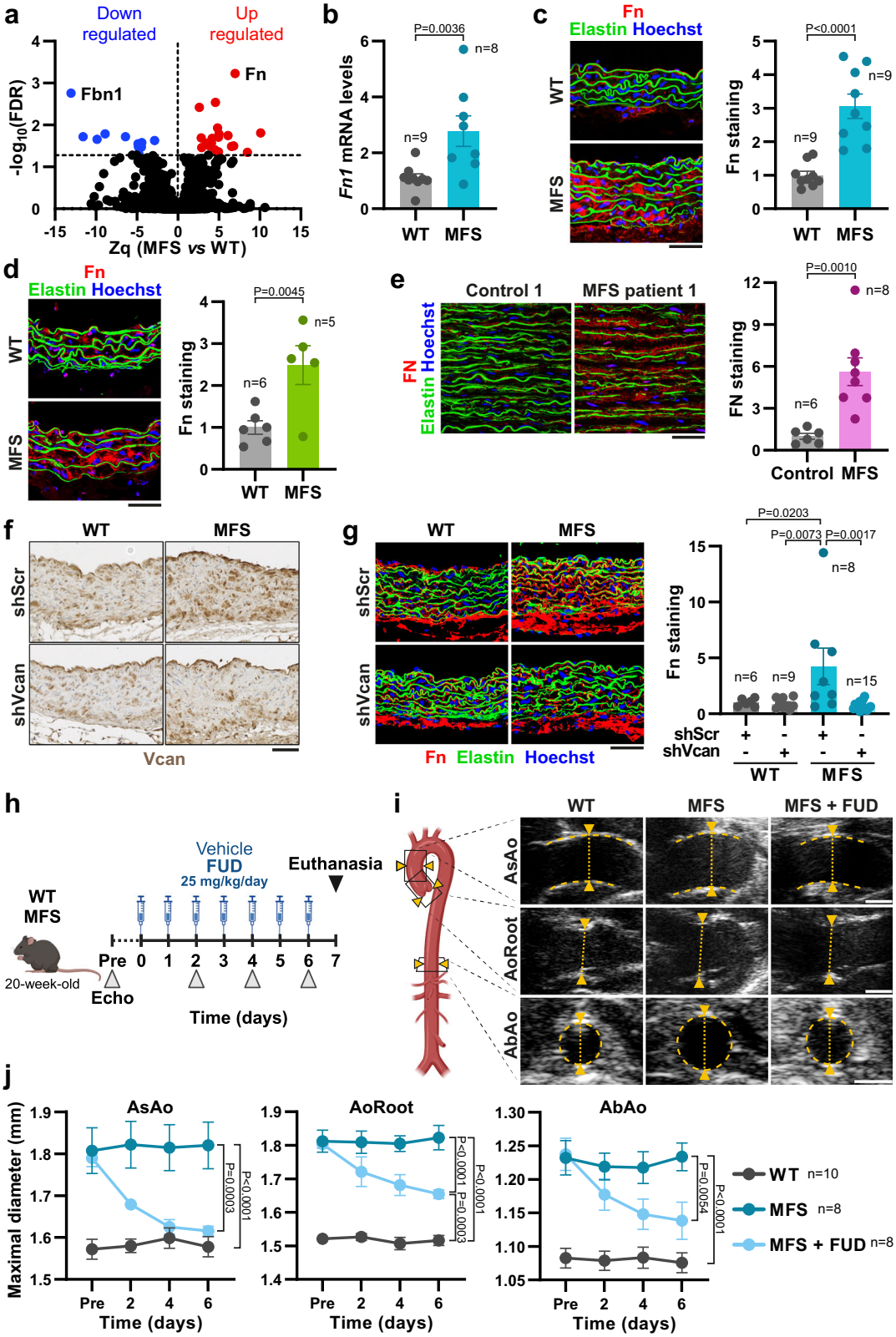

evidenced by normalized Nos2 and pVasp^{S239} levels in the aorta of MFS mice (Fig. 2a).

To test whether FN directly activates this pathway, aortic rings were incubated with FN for 6 h. Immunofluorescence revealed FN penetration into the aortic medial layer and induction of Nos2 and pVasp^{S239} to levels comparable to those in MFS rings (Fig. 2b, c). Our recent studies revealed that Vcan accumulation in the aorta induces Nos2 expression and drives MFS aortic disease via Akt activation[13]. To assess whether FN also induces Nos2 via this pathway, VSMCs were cultured for 1 h on plates coated with FN or collagen, which is also elevated in the aorta of MFS[26]. FN specifically activated Akt, as indicated by phosphorylation at S473, and induced Nos2 expression and NO overproduction (Supplementary Figs. 5a–c). Moreover, FN also increased pVasp^{S239} staining (Supplementary Fig. 5d), consistent with Pkg activation.

Fig. 1 | Fibronectin accumulation in MFS aortas mediates aortic dilation. **a** Volcano plot from proteomic analysis of AsAo from 12-week-old WT and MFS mice ($n = 6$ pools of 2 aortas per group), showing relative protein abundance (Zq) versus false discovery rate (FDR). **b** RT-qPCR analysis of *Fn1* expression in 9 WT and 8 MFS aortas from 12-week-old male mice. mRNA amounts were normalized to *Gapdh* and expressed relative to WT. Each point denotes one mouse. Data are mean ± s.e.m. **c**–**e** Representative FN immunofluorescence (red), elastin autofluorescence (green), and Hoechst-stained nuclei (blue) with quantification in aortic tissue from 12-week-old (**c**) male WT and MFS mice, (**d**) female WT and MFS mice, and (**e**) control donors and MFS patients. Scale bar, 50 µm. Data are shown relative to WT mice or control donors (mean ± s.e.m.); each point denotes one individual ($n = 5$–9 as indicated). **f** Representative Vcan immunohistochemistry in aortic tissue from WT and MFS mice treated with shScr or shVcan lentivirus ($n = 8$, 9, 8, 20 mice for WT shScr, WT shVcan, MFS shScr, and MFS ShVcan, respectively). Scale bar, 50 µm. **g** Fn immunofluorescence (red), elastin autofluorescence (green), and Hoechst-stained nuclei (blue) with quantification in aortas from WT and MFS mice treated with shScr or shVcan lentivirus. Scale bar, 50 µm. Data are shown relative to WT shScr (mean ± s.e.m.); each point denotes one individual ($n = 6$–15 as indicated). **h** Experimental design. **i** Aorta scheme and representative in vivo ultrasound images of AsAo, AoRoot, and AbAo from 20-week-old WT, untreated MFS, and FUD-treated MFS mice at day 6. Measurement regions and lumen diameters are indicated. Scale bar, 1 mm. **j** Maximal AsAo, AoRoot, and AbAo diameters over time in WT, MFS, and FUD-treated MFS mice ($n = 8$–10 as indicated). Data are mean ± s.e.m. Statistical significance was assessed by one-sided unpaired Student's *t* test (**b**–**e**), one-way ANOVA with Tukey's post-hoc test (**g**), or repeated-measures (RM) two-way ANOVA with Tukey's post-hoc test (**j**). **h** and the aorta scheme in **i** were created in BioRender. Martin, N. (2026) https://BioRender.com/yi4yh4f). Source data are provided as a Source Data file.

Given the critical contribution of contractility dysregulation to TAAD, myography was employed to assess whether FN affected the contractile capacity of the aorta. Endothelium-denuded aortic rings from WT mice were used in these assays to avoid interference from the NO derived from endothelium-specific Nos3. Addition of FN to the aortic rings nearly blocked noradrenaline-induced contractility (Fig. 2d). Notably, this effect of FN was prevented in the presence of either FUD or the Nos2-specific inhibitor 1400 W (Fig. 2d). Collectively, these results support the notion that the pathological effects of FN accumulation in the aorta are mediated by overactivation of the NO canonical signaling pathway (Fig. 2e).

Finally, because FN can act via surface interactions or stiffness-dependent cues, we assessed the effects of substrate stiffness by culturing cells on FN-coated polyacrylamide (PAAm) hydrogels spanning a low-stiffness (2 kPa) and a high-stiffness (112 kPa) range, representing compliant and pathological aortic environments, respectively. NO production did not differ between mVSMCs cultured on soft versus stiff hydrogels (Supplementary Fig. 5e). Given that Nos2 expression and NO production were induced by FN-coated, but not by collagen-coated, high-stiffness surfaces (Supplementary Fig. 5b, c), these findings strongly suggest that FN-driven signaling, rather than increased matrix stiffness per se, drives activation of the NO pathway in MFS.

The $\alpha_V\beta_3$ integrin mediates aortic disease in MFS

After demonstrating the pathogenic effect of FN accumulation, we sought to identify the specific FN receptor mediating this effect. TLR-4, CD44, Syndecan-4, and at least 12 integrins can serve as FN receptors and therefore mediate its contribution to aortopathy in MFS[27–30]. Previous studies suggested that the integrin $\alpha_5\beta_1$ mediates aortopathy in MFS[31]; however, considering its involvement in FN fibrillogenesis[32,33], current evidence suggests that its contribution to aortic disease may involve facilitating FN accumulation rather than directly influencing downstream events[31]. Additionally, it has been suggested that the integrin $\alpha_V\beta_3$ mediates aortic disease in MFS[34], but the evidence is based on the inhibitory effect on aortic growth of an integrin blocker that inhibits not only α_V-containing integrins but also $\alpha_5\beta_1$[35].

To investigate whether any of the integrins expressed on VSMCs ($\alpha_3\beta_1$, $\alpha_5\beta_1$, $\alpha_8\beta_1$, $\alpha_V\beta_1$, and $\alpha_V\beta_3$) mediate NOS2 induction by FN, we used lentivirus encoding shRNAs specific to *ITGAV* (shITGAV) or *ITGB1* (shITGB1), and a lentivirus encoding a non-specific shRNA sequence (shScr) as control, to specifically and efficiently knockdown the expression of these integrins in human VSMCs (Supplementary Fig. 6a). We performed these experiments in human umbilical artery SMCs (HUASMCs), which were available in our laboratory, and because FN-induced NOS2 expression was expected to be independent of the arterial origin of the SMCs. Unlike transduction with shScr or shITGB1, silencing *ITGAV* blocked NOS2 induction in HUASMCs cultured on FN (Fig. 3a), suggesting that $\alpha_V\beta_3$ is the integrin responsible for mediating this response. Supporting this hypothesis, a neutralizing antibody (Ab) against mouse α_V prevented FN-induced aortic contractility impairment, while a neutralizing Ab against mouse β_1 integrin did not (Fig. 3b). Consistently, in HUASMCs, a neutralizing Ab targeting $\alpha_V\beta_3$ blocked FN-induced AKT activation, NOS2 induction, and NO overproduction (Fig. 3c–e), further supporting the notion that this integrin mediates the pathogenic role of FN in MFS aortopathy. Importantly, this neutralizing Ab also blocked NOS2 expression and NO overproduction in human aortic VSMCs (Supplementary Fig. 6b, c), suggesting that FN signaling through $\alpha_V\beta_3$ occurs independently of VSMC origin.

Consistent with these functional data, immunostaining of aortic sections unveiled increased levels of the α_V integrin subunit and the $\alpha_V\beta_3$ heterodimer in the aortic medial layer of MFS patients relative to control donors (Fig. 3f and Supplementary Figs. 7 and 8). Similarly, staining of the α_V and β_3 subunits, or the $\alpha_V\beta_3$ heterodimer in AsAo sections of MFS mice, showed upregulation relative to control littermates (Fig. 3g and Supplementary Fig. 6d). These findings strongly suggest that the signaling leading to MFS aortopathy by FN accumulation may be mediated by the $\alpha_V\beta_3$ integrin.

To further challenge this hypothesis, we used a cyclic pentapeptide, c(RGDyK), which selectively impairs the interaction of the $\alpha_V\beta_3$ integrin with its substrates[36] (Supplementary Table 2). Immunoblot and immunofluorescence analyses showed that c(RGDyK) prevented FN-induced Akt activation (Supplementary Fig. 9a), Nos2 induction, NO overproduction, and Pkg overactivation (Supplementary Fig. 9b) in mouse VSMCs. Moreover, this peptide also prevented the loss of aortic contractility induced by FN in aortic rings as efficiently as the Nos2 inhibitor 1400 W (Supplementary Fig. 9c).

Given the contribution of NO pathway overactivation and aortic contractility dysregulation to aortopathy in MFS, we conducted in vivo experiments to assess whether the inhibition of the $\alpha_V\beta_3$ integrin interaction with FN could reverse the MFS-associated aortopathy. MFS male mice were treated with c(RGDyK) for 6 consecutive days using osmotic minipumps, and aortic diameters were monitored by echography before and on days 1, 3, and 6 after starting the treatment (Fig. 4a). Treatment with c(RGDyK) reduced the AsAo diameter to normal values, completely reversing local dilation, and substantially decreased AoRoot and AbAo diameters (Fig. 4b). Immunostaining revealed that the reduction in aortic enlargement was accompanied by the reversion of Nos2 induction and Pkg overactivation (Fig. 4c).

MFS aortas exhibit hallmarks of biomechanical dysfunction such as increased Pulse Wave Velocity (PWV)[37], as well as structural deterioration manifested as medial degeneration, characterized by elastic-fiber fragmentation and disarray[14,38]. To determine whether the c(RGDyK) peptide could reverse medial degeneration, we stained aortic cross sections from MFS mice after 28 days of treatment with the peptide using modified Verhoeff elastic-Van Gieson (EVG) (Fig. 4d). Remarkably, this treatment normalized aortic diameter and AsAo PWV in male MFS mice (Fig. 4e–g) and reduced elastic-fiber fragmentation and plasma nitrite levels (Fig. 4h, i), consistent with normalization of

https://doi.org/10.1038/s41467-026-74707-4

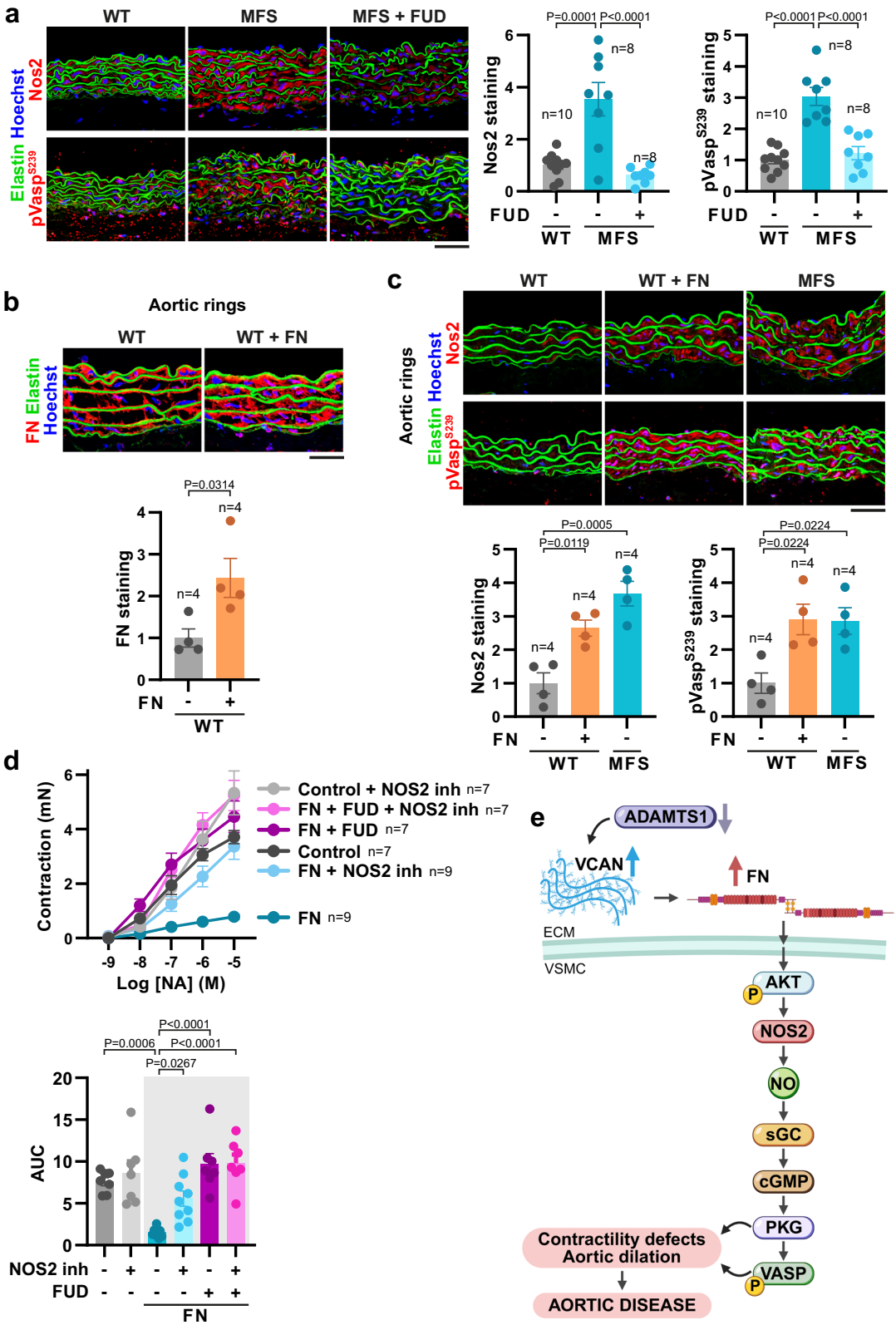

Nos2 expression. Notably, reversal of aortopathy through inhibition of FN-$\alpha_V\beta_3$ interaction did not normalize Fn levels in the aorta (Supplementary Fig. 10a), and no evidence of hyperplasia was observed in any experimental group (Supplementary Fig. 10b).

Consistent effects were observed in female MFS mice. Twenty-eight days of c(RGDyK) administration reversed aortic dilation and reduced AsAo PWV and plasma nitrite levels (Fig. 5a–e). Histological analysis further revealed decreased elastin fragmentation and normalization of Nos2 expression and pVasp^{S239} levels, again without altering Fn accumulation in the aortic media (Fig. 5f–h).

Together, these findings support a model in which FN accumulation, likely facilitated by $\alpha_5\beta_1$-mediated FN polymerization, triggers MFS aortopathy by overactivating the NO pathway through the $\alpha_V\beta_3$ integrin (Fig. 5i).

Fig. 2 | Fibronectin impairs aortic contractility through Nos2 induction. **a** Representative images and quantification of Nos2 (top) or pVasp^{S239} (bottom) immunofluorescence (red) in aortic sections of 10 WT, 8 MFS, and 8 FUD-treated MFS 20-week-old male mice. Elastin autofluorescence (green) and Hoechst-stained nuclei are shown. Scale bar, 50 µm. Data are expressed relative to WT as mean ± s.e.m. Each point denotes one mouse. **b** Representative images and quantification of FN immunofluorescence (red) in aortic tissue from 12-week-old mice after incubation of aortic rings for 6 h with vehicle or FN. Elastin autofluorescence (green) and Hoechst-stained nuclei (blue) are shown. Scale bar, 50 µm. Data are shown relative to control rings as mean ± s.e.m. Each point denotes one ring ($n = 4$ per group). **c** Representative images and quantification of Nos2 or pVasp^{S239} immunofluorescence (red) in aortic rings from 12-week-old WT and MFS mice after 6 h incubation with vehicle or FN. Elastin autofluorescence (green) and Hoechst stained nuclei (blue) are shown. Scale bar, 50 µm. Data are shown relative to control WT rings as mean ± s.e.m. Each point denotes one ring ($n = 4$ per group). **d** Contractile responses of endothelium-denuded aortas to L-noradrenaline (NA) (top) and area under the curve (AUC; bottom) after 6 h incubation with vehicle or FN (40 µg/ml). Where indicated, the FN inhibitor FUD (40 µg/ml) or the NOS2-inhibitor 1400 W (10 µM) was added. Data are mean ± s.e.m. ($n = 7–9$ as indicated); each point (bottom panel) represents one mouse aorta. **e** Schematic model of FN-induced activation of NO signaling in MFS; created in BioRender. Martin, N. (2026) https://BioRender.com/yi4yh4f). ADAMTS1 downregulation in MFS promotes VCAN accumulation and subsequent FN deposition. FN indirectly induces AKT activation, leading to NOS2 overexpression, NO overproduction, sGC activation, and subsequent cGMP production. High cGMP levels overactivate PKG, which phosphorylates VASP. PKG and pVASP drive contractility impairment and aortic dilation, promoting aortic disease. Statistical significance was assessed by one-way ANOVA with Tukey's post-hoc test (**a**, **c**, **d**) or one-sided unpaired Student's *t* test (**b**). Source data are provided as a Source Data file.

FN-$\alpha_V\beta_3$ activates the AKT-NOS2 pathway in MFS via PI3K-PIP3-PDK1-ILK

Given the effects of FN accumulation on AKT activation, we investigated the signaling events leading to AKT activation triggered by FN-$\alpha_V\beta_3$ in MFS. Since Focal Adhesion Kinase (FAK) complexed with SRC family kinases and Integrin-Linked Kinase (ILK) could potentially mediate AKT activation by FN-$\alpha_V\beta_3$ (Fig. 6a), we first assessed their activation state in MFS aortas.

To evaluate FAK activation, we measured the level of FAK autophosphorylation at Y397, a canonical marker of integrin-induced FAK activation[39]. Immunostaining of aortic cross-sections showed that pFAK^{Y397} was reduced in MFS aortas compared to controls in both human and mice (Fig. 6b, c, and Supplementary Fig. 11). Immunoblotting of aortic extracts also showed a reduction in the pFak^{Y397}/Fak ratio in MFS mice relative to control littermates (Supplementary Fig. 12a). Moreover, the FAK-specific inhibitor defactinib and the SRC-specific inhibitor dasatinib (Supplementary Table 2) failed to rescue the loss of contractility induced by adding FN to the aortic rings (Fig. 6d and Supplementary Fig. 12b). Consistently, defactinib and dasatinib did not prevent Nos2 induction by FN in VSMCs (Supplementary Fig. 12c). However, dasatinib effectively inhibited Src, as evidenced by the inhibition of Src-induced Fak phosphorylation at Y576/Y577, whereas defactinib effectively inhibited Fak autophosphorylation at Y397 (Fig. 6e and Supplementary Fig. 12d). Collectively, these results strongly suggest that FAK does not mediate the pathological overactivation of the NO pathway nor the effects on aortic contractility resulting from FN accumulation in MFS.

In contrast, ILK signaling was markedly dysregulated. Immunofluorescence analysis revealed increased ILK protein levels in aortic tissue from MFS patients compared with control donors (Fig. 6f and Supplementary Fig. 13). While total Ilk levels did not substantially increase in the aortic tissue of 20-week-old MFS mice (Supplementary Fig. 14a), Ilk phosphorylation at S343, an essential event for ILK activation and subsequent interaction with AKT[40], showed a marked increase in both male and female MFS mice (Fig. 6g and Supplementary Fig. 14b). Notably, treatment of MFS mice with the $\alpha_V\beta_3$ integrin inhibitor c(RGDyK) reversed Ilk^{S343} phosphorylation to WT levels (Fig. 6g and Supplementary Fig. 14b), and FN treatment induced pIlk^{S343} in aortic rings (Supplementary Fig. 14c). Moreover, in contrast to Fak or Src inhibition, Ilk inhibition with its specific inhibitor ILK-IN-2 (Supplementary Table 2) prevented the loss of contractility induced by adding FN to the aortic rings (Fig. 6h). Additionally, this inhibitor also prevented Nos2 induction as well as Pkg and Akt overactivation by FN in VSMCs (Fig. 6i, j). These results strongly suggest that, unlike FAK, ILK is a critical mediator of NO signaling pathway overactivation by FN-$\alpha_V\beta_3$.

To gain insight into the mechanisms of ILK-mediated AKT activation by FN-$\alpha_V\beta_3$, we focused on PI3K. PI3K-generated phosphatidylinositol 3,4,5-triphosphate (PIP3) recruits AKT, PDK1, and ILK to the membrane, promoting PDK1- and ILK-mediated AKT activation through its phosphorylation at T308 and S473, respectively[41,42]. We hypothesized that PI3K-mediated activation of PDK1 and ILK may be essential for the overactivation of the NO signaling pathway and aortic contractility dysregulation (Fig. 7a). To test this hypothesis, we evaluated the effect of specific inhibitors of PI3K (Wortmannin) and PDK1 (GSK2334470), as well as an inhibitor of PIP3-mediated membrane recruitment of ILK, AKT, and PDK1 (PIT-1) (Supplementary Table 2), on the contractile response of aortic rings treated with FN. Similar to Nos2 inhibition with 1400 W, wortmannin, PIT-1, and GSK2334470 prevented the loss of contractility induced by adding FN to aortic rings (Fig. 7b–d). These inhibitors also blocked Akt activation in VSMCs and aortic rings (Fig. 7e, f) and suppressed Nos2 induction and NO overproduction in VSMCs (Fig. 7g), suggesting that PI3K-mediated generation of PIP3 and activation of ILK and PDK1 are indispensable for FN-$\alpha_V\beta_3$-induced pathogenic signaling and contractility dysregulation in MFS.

Consistent with the moderate phenotype of *Fbn1*$^{C1041G/+}$ mice, no mortality or aortic rupture was observed in untreated mice. To assess the relevance of this signaling pathway in more severe forms of MFS and in other TAAD models, we performed immunofluorescence analyses for Fn, α_V, $\alpha_V\beta_3$, pIlk^{S343}, and Nos2 in aortas from *Fbn1*$^{mgR/mgR}$ MFS mice (mgR mice), a model that develops lethal aortic dissections, as well as from WT mice treated with β-aminopropionitrile (BAPN) and angiotensin II (AngII). Robust activation of the pathway was observed in mgR aortas (Supplementary Fig. 15a). In contrast, despite the marked severity of disease in the BAPN+AngII model, where 3 of 8 mice experienced lethal aortic rupture and 4 additional animals developed large aneurysms in the AsAo and/or AbAo, these signaling mediators were not upregulated (Supplementary Fig. 15b, c). Together, these findings suggest that activation of the FN-$\alpha_V\beta_3$-ILK-NO signaling pathway is a defining feature of genetically driven MFS aortopathy, but not of pharmacologically induced TAAD models.

PDK1 and ILK are essential mediators of aortic disease in MFS

To define the contribution of PDK1 to MFS aortopathy, MFS mice were treated for 6 days with the PDK1 inhibitor GSK2334470 delivered via osmotic minipumps (Fig. 8a). Pdk1 inhibition reversed aortic dilation and restored NA-induced contractility (Fig. 8b, c). However, short-term ex vivo incubation of MFS aortic rings with GSK2334470 for 6 h failed to improve contractile responses (Supplementary Fig. 16a), suggesting that recovery of aortic contractile function requires sustained inhibition over longer periods rather than acute exposure.

Similarly, to investigate the potential contribution of ILK to MFS-related aortopathy, we administered the ILK-IN-2 inhibitor to MFS mice for 6 consecutive days (Fig. 8d). This treatment readily reversed AsAo and AoRoot dilation in MFS mice within this brief timeframe (Fig. 8e). Moreover, immunofluorescence analysis of aortic cross-sections revealed that ILK-IN-2 treatment reversed Nos2 induction and Pkg

https://doi.org/10.1038/s41467-026-74707-4

overactivation in MFS mice (Fig. 8f). However, ILK-IN-2 treatment was associated with a high mortality rate, with 50% of mice dying by day 6, and a small reduction in body weight (Supplementary Fig. 16b, c). These adverse effects prompted us to seek alternative strategies to further investigate the role of ILK in MFS pathogenesis in vivo.

First, we selected a lentiviral vector encoding green fluorescent protein (GFP), to monitor transduction efficiency, and either a non-specific shRNA (shScr) or an *Ilk*-specific shRNA (shIlk) that readily decreased *Ilk* mRNA levels in cultured VSMCs (Supplementary Fig. 17). To silence Ilk in vivo in aortas, these lentiviruses were inoculated by intrajugular vein injection[43,44] in 14-week-old MFS mice (Fig. 9a). After lentivirus delivery, we monitored AsAo, AoRoot, and AbAo diameters weekly for 28 days, noting a complete reversal of AsAo, AoRoot, and AbAo dilation (Fig. 9b). This reversion of the aortic dilation was

Fig. 3 | $\alpha_V\beta_3$ integrin is upregulated in MFS aortas and mediates NOS2 induction by FN. a HUASMCs were transduced with control (shScr), *ITGAV*-targeting (sh*ITGAV*), or *ITGB1*-targeting (sh*ITGB1*) shRNAs, serum-starved and seeded for 1 h on plates coated with collagen/poli-L-lysine (Control) or FN. Representative images and quantification of NOS2 immunofluorescence (red) are shown. Nuclei were stained with Hoechst (blue). Scale bar, 100 µm. Data are presented relative to Control as mean ± s.e.m. Each point denotes an independent experiment ($n = 4$ per group). **b** Contractile responses to NA in endothelium-denuded aortas and AUC after 6 h incubation with vehicle or FN. Control IgG or neutralizing Abs against α_V or β_1 integrins were added as indicated. Data are shown as mean ± s.e.m (both panels). Each point represents one mouse aorta ($n = 5$–8 as indicated). **c** Representative immunoblots and quantification of AKT phosphorylation ($pAKT^{S473}$/total AKT) in HUASMCs seeded on collagen or FN for 1 h in the presence of a neutralizing $\alpha_V\beta_3$ integrin Ab or control IgG. Data are shown relative to control as mean ± s.e.m. Each point denotes an independent experiment ($n = 3$ per group). Representative images and quantification of NOS2 immunofluorescence (**d**, red) and NO staining (**e**, green), in HUASMCs seeded on collagen or FN with $\alpha_V\beta_3$-blocking Ab or control IgG. Scale bar, 100 µm. Data are mean ± s.e.m. Each point denotes an independent experiment ($n = 6$ in **d**; $n = 5$ in **e**). Representative images and quantification of α_V, β_3, and $\alpha_V\beta_3$ integrin staining in the medial layer of aortic tissue from control donors and MFS patients (**f**) and from 20-week-old WT and MFS male mice (**g**). Scale bar, 50 µm. Data are mean ± s.e.m. Each point denotes one individual or mouse ($n = 7$–9). Elastin autofluorescence (green) and Hoechst-stained nuclei (blue) are shown. Statistical significance was assessed by one-way ANOVA with Tukey's post-hoc test (**a**–**e**) or one-sided unpaired Student's *t* test (**f**, **g**). Source data are provided as a Source Data file.

accompanied by a recovery of the aortic wall structure, evidenced by a reduction in elastic fiber fragmentation 28 days after lentiviral administration (Fig. 9c). Immunostaining of AsAo sections 28 days after lentivirus injection confirmed the expression of GFP in infected mice (with shScr or shIlk-encoding lentivirus) and a substantial reduction in Ilk levels only in mice injected with shIlk-encoding lentivirus (Fig. 9d). Corresponding with the reversal of medial layer degeneration and aortic dilation, *Ilk* silencing in MFS mice led to reversal of Nos2 induction and Pkg overactivation (Fig. 9e).

The normalization of aortic contractility by ILK-IN-2 in endothelium-denuded aortic rings suggested that ILK expressed in VSMCs mediated aortopathy in MFS. To test this hypothesis, we generated MFS mice with specific, tamoxifen (TX)-inducible *Ilk* deletion in smooth muscle cells (SMCs) (*Fbn1*$^{C1041G/+}$;*Ilk*$^{flox/flox}$;*Myh11-Cre*^{ERT2} mice) by crossing *Fbn1*$^{C1041G/+}$ mice with *Ilk*$^{flox/flox}$ mice[45] and *Myh11-Cre*^{ERT2} mice, which express a modified version of the Cre recombinase inducible by TX[46]. This genetic approach enabled the specific deletion of *Ilk* in SMCs of 4-week-old mice following 5 consecutive days of TX administration. We monitored aortic diameter before and after TX administration, weekly for 28 days (Fig. 10a), and found that *Ilk* deficiency conferred protection against dilation of the AsAo, AoRoot, and AbAo in young MFS mice, reaching normal diameters in AsAo and AbAo (Fig. 10b). After verifying the marked reduction in Ilk expression in animals administered TX (Fig. 10c), we studied the main pathological features of MFS aortas. Consistent with the prevention of aortic enlargement, *Ilk*-deficient MFS aortas showed a marked reduction in Nos2 induction and Pkg overactivation (Fig. 10d), and a recovery of elastic fiber integrity (Fig. 10e). Additionally, *Ilk* deficiency in SMCs restored the contractile capacity in MFS aortas (Fig. 10f). These results highlight the crucial role of Ilk in the development and progression of MFS aortic disease.

Discussion

In this study, we have identified a previously unrecognized molecular mechanism underlying TAAD in MFS, which holds promise as a potential target for robust pharmacotherapies. The development of these therapeutic strategies is imperative for effectively managing MFS patients, given the current absence of medical treatments capable of preventing pathological aortic dilation or dissection, thereby leaving surgical repair as the primary option to prevent aortic events.

Our previous studies revealed that overactivation of the NO pathway, driven by AKT-mediated induction of NOS2 in VSMCs, mediates MFS-associated aortopathy[13–15]. In the present study, we have demonstrated that the ECM protein FN accumulates in the aortas of *Fbn1*$^{C1041G/+}$ mice of 12 and 24 weeks of age and in MFS patients across a range of ages and that this accumulation contributes to the aortic disease. Furthermore, we have extensively delineated the molecular mechanism by which FN induces aortic disease in MFS. Our findings strongly suggest that accumulated FN initiates a signaling cascade through the $\alpha_V\beta_3$ integrin, involving PI3K and PIP3, and resulting in ILK overactivation. This overactivation subsequently induces AKT phosphorylation at S473, thereby activating AKT. These findings establish the most comprehensive signaling pathway implicated in MFS aortopathy to date, connecting aortic ECM alterations with the AKT-NO cascade through integrin-mediated signaling, and unveil several actionable targets for therapeutic intervention in MFS (Fig. 7a).

Our data demonstrate that FN accumulates in the aortas of MFS patients and mice, in both sexes. These findings align with previous reports of elevated FN expression in the tunica media of both syndromic and non-syndromic thoracic aortic aneurysms (TAA) in humans and mice[31,47,48]. Whether this accumulation was merely a consequence of the disease or played a causative role remained unknown. Here we show that Fn accumulation correlates with increased levels of Vcan, an ADAMTS1 substrate previously shown to accumulate in MFS aortas and to drive disease by inducing Nos2 through Akt activation[13]. *Vcan* haploinsufficiency protects MFS mice against aortic dilation[13], consistent with our prior report showing that *Adamts1* deficiency causes a syndromic aortic phenotype similar to MFS and that ADAMTS1 protein levels are markedly reduced in both MFS mice and patients[14]. Strikingly, *Vcan* silencing not only reverses MFS aortopathy but also strongly reduces Fn levels to those observed in WT mice, suggesting a regulatory link whereby Vcan governs Fn abundance. Thus, Fn accumulation in MFS may occur secondary to Vcan elevation resulting from Adamts1 deficiency, a hypothesis further supported by evidence that VCAN directly interacts with FN and promotes its assembly and accumulation[49].

Because FN exists in the ECM as inactive dimers and biologically active multimeric fibrils[19,20], we used the fibronectin assembly inhibitor FUD, a peptide that disrupts FN-FN interactions[21,22], to assess the specific contribution of active FN to MFS aortopathy. Although a 7-day in vivo treatment was insufficient to reduce total FN abundance within the aortic wall, likely reflecting the slower kinetics of ECM turnover, it was nevertheless sufficient to suppress aberrant activation of the NO pathway and to disengage elastic fibres from a FN- and collagen-enriched ECM. This ECM remodeling was accompanied by a substantial reduction in aortic stiffness. Importantly, FUD treatment also reversed aortic dilation and normalized aortic contractile responses, demonstrating that interfering with FN fibrillogenesis is sufficient to rescue key structural and functional hallmarks of MFS aortic disease. Collectively, these findings provide strong evidence that accumulation of fibrillar FN is a pathogenic driver of aortic disease in MFS.

We also identified the receptor mediating the pathogenic effects of FN. TLR-4, CD44, Syndecan-4, and at least 12 integrins can serve as FN receptors and thus potentially mediate their contribution to aortopathy in MFS[27–30]. Among FN-binding integrins, $\alpha_5\beta_1$ plays a central role in inducing FN conformational changes that promote fibrillogenesis and matrix deposition[32,33]. Indeed, its genetic impairment prevents FN accumulation and limits aneurysm progression in the *Fbn1*$^{mgR/mgR}$ mouse model of MFS[31]. However, our data indicate that β_1 integrins do not mediate FN-induced NO pathway overactivation or the associated contractile dysfunction. Instead, we identify integrin

https://doi.org/10.1038/s41467-026-74707-4

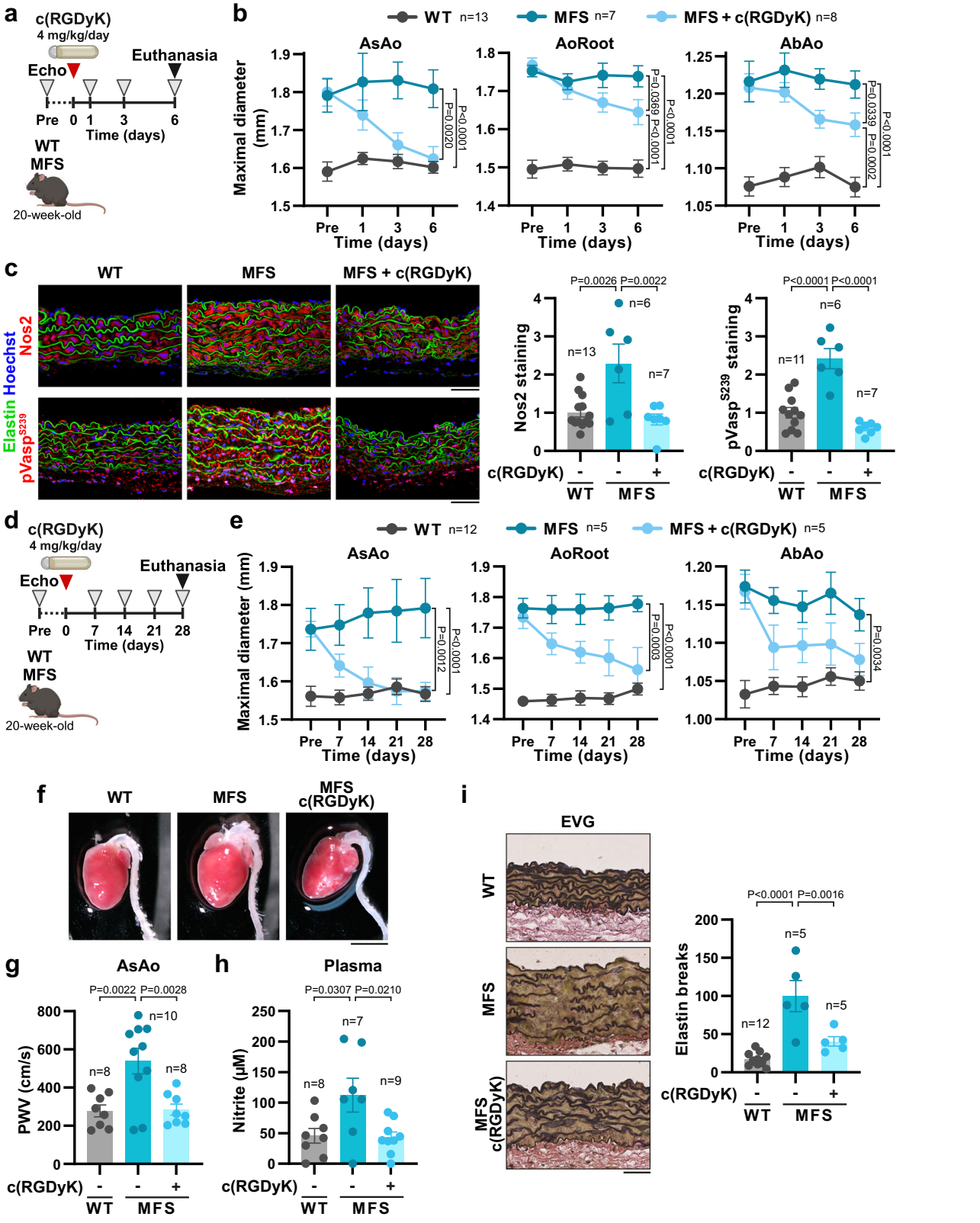

$\alpha_V\beta_3$ as the critical transducer of these downstream pathogenic effects. This conclusion is supported by the ability of α_V silencing, $\alpha_V\beta_3$-neutralizing Abs, and the $\alpha_V\beta_3$-specific inhibitor c(RGDyK) to suppress NOS2 induction, NO production, PKG overactivation, and FN-induced impairment of VSMC and aortic contractility. These findings are consistent with previous reports showing that signaling through $\alpha_V\beta_3$ integrin triggers VASP phosphorylation and activation in fibroblasts[50].

Together, our results support a model in which $\alpha_5\beta_1$ integrin primarily facilitates FN accumulation within the MFS aortic wall, whereas $\alpha_V\beta_3$ transduces FN-dependent NO signaling that drives contractile dysfunction and aortic disease. In line with this model, pharmacological inhibition of $\alpha_V\beta_3$ using c(RGDyK) was sufficient to reverse aortic disease in MFS mice, yet, unlike impairment of $\alpha_5\beta_1$, did not alter aortic FN abundance in the aorta.

Fig. 4 | $\alpha_V\beta_3$ integrin/FN interaction mediates NO pathway activation and aortic disease in male MFS mice. a Experimental design for short-term treatment: 20-week-old male MFS mice were treated for 6 days with c(RGDyK). Sham-operated WT and MFS mice were used as controls. **b** Maximal AsAo, AoRoot, and AbAo diameters over time in WT, MFS, and c(RGDyK)-treated MFS mice ($n = 7–13$ as indicated). Data are mean ± s.e.m. **c** Representative images and quantification of Nos2 or pVasp^{S239} immunofluorescence (red) in aortic sections from WT, MFS, and c(RGDyK)-treated MFS mice after 6 days of treatment. Scale bar, 50 µm. Data are shown relative to WT as mean ± s.e.m. Each point denotes one mouse (n = 6–13 as indicated). **d** Experimental design for long-term treatment: 20-week-old MFS male mice were treated 28 days with c(RGDyK). Sham-operated WT and MFS mice were used as controls. **e** Maximal AsAo, AoRoot, and AbAo diameters over time in WT, MFS, and c(RGDyK)-treated MFS mice ($n = 5–12$ as indicated). Data are mean ± s.e.m. **f** Representative gross morphology of thoracic aortas at study end point. Scale bar, 500 µm. PWV of the AsAo (**g**) and plasma nitrate plus nitrite levels (**h**) in WT, MFS, and c(RGDyK)-treated MFS mice ($n = 7–10$ as indicated). Data are mean ± s.e.m. **i** Representative elastic van Gieson (EVG) staining and quantification of elastin breaks per aortic section in aortas after 28 days of treatment. Scale bar, 50 µm. Data are mean ± s.e.m. Each point denotes one mouse ($n = 5–12$ as indicated). Statistical significance was assessed by RM two-way ANOVA with Tukey's post-hoc test (**b**, **e**) or one-way ANOVA with Tukey's post-hoc test (**c**, **g**–**i**). **a**, **d** These were created in BioRender. Martin, N. (2026) https://BioRender.com/yi4yh4f). Source data are provided as a Source Data file.

Although the involvement of this integrin in MFS aortic disease had been suggested[34], evidence supporting this hypothesis was based on the mere observation that the broad-spectrum α_V blocker GLPG0187 prevented aortic growth in MFS mice[34]. Additionally, it should be noted that this compound inhibits not only α_V-containing integrins but also $\alpha_5\beta_1$[35]. Consequently, the reported effects could be attributed to $\alpha_5\beta_1$ or any of several α_V-containing integrins. Moreover, $\alpha_V\beta_3$ upregulation may not represent a universal feature of all forms of TAAD. Indeed, a recent study reported reduced α_V expression in aortic samples from non-MFS TAAD patients[51]. However, this observation should be interpreted with caution, as integrin expression is likely to differ substantially between aneurysmal tissue and fully dissected aortas, where extensive inflammation and VSMC loss are prominent[52]. Importantly, the same study showed that prolonged inhibition of α_V integrins using cilengitide or SB273005 exacerbated TAA development in the BAPN model. Notably, these inhibitors were administered for six weeks beginning at 3 weeks of age, a critical developmental period during which the aorta is still undergoing postnatal growth (see Fig. 10b). This raises the possibility that early-life integrin inhibition exerts effects that are distinct from those observed when integrin signaling is targeted in the adult aorta.

Our previous findings indicated that AKT was overactivated in the aortas of MFS patients and that its inhibition reversed Nos2 induction and aortic dilation in MFS mice[13]. We now provide mechanistic evidence strongly suggesting that FN-$\alpha_V\beta_3$ induces the AKT-NO signaling pathway via a mechanism involving PI3K, PIP3, PDK1, and ILK (Fig. 7a). A recent study proposed that AKT may be activated by FAK in MFS[34]. However, this hypothesis was primarily supported by evidence from in vitro experiments conducted with induced pluripotent stem cells (iPSC)-derived SMCs exhibiting a phenotype akin to second heart field (SHF)-derived SMCs. The study also suggested that the broad-spectrum integrin blocker GLPG0187 inhibited AKT phosphorylation at T308, implicating either FAK, as suggested in that study, or PDK1, as we propose, as potential mediators of this event. Our findings revealing FAK activity downregulation not only in the AsAo of MFS mice, primarily populated by neural crest-derived SMCs, but also in human MFS AoRoot specimens predominantly populated by SHF-derived SMCs, support the notion of PDK1-mediated AKT activation. Additionally, the ineffectiveness of pharmacological FAK inhibition in attenuating FN-induced Nos2 overexpression and Pkg overactivation in VSMCs, or in restoring contractile capacity in FN-treated aortas, further strengthens the argument against FAK involvement in MFS aortic disease signaling induced by FN. In contrast, our findings strongly support the notion that ILK and PDK1 mediate the pathological signaling induced by FN and $\alpha_V\beta_3$ integrin, along with the overactivation of the NO pathway in MFS aortas, with the involvement of PI3K and PIP3. Indeed, we observed increased ILK expression in the aortas of MFS patients and Ilk overactivation in the aortas of MFS mice relative to controls. Additionally, contrary to FAK or SRC inhibitory drugs, a pharmacological ILK inhibitor prevented Nos2 induction, Pkg overactivation, and aortic contractility impairment by FN. These findings are consistent with previous reports showing that the ILK-AKT pathway induces NOS2 expression and NO production in LPS-stimulated macrophages[53] and TNFα-stimulated myoblasts[54]. Further supporting our hypothesis, drugs that inhibit the activity of PI3K or PDK1, or a drug that blocks PIP3-mediated recruitment of ILK, PDK1, and AKT to the plasma membrane, all suppressed NO pathway overactivation and aortic contractility dysregulation induced by FN. Notably, in vivo inhibition of PDK1 reversed aortic dilation and restored aortic contractile activity in MFS mice. Also in line with our findings, previous studies indicated that ILK negatively regulates VSMC contraction independently of integrin β_1[55], though the specific pathological mechanism and the role of specific integrins remained poorly understood. PDK1, once activated by PI3K, phosphorylates AKT at T308[56,57], which facilitates the subsequent ILK-dependent phosphorylation of AKT at S473, achieving its complete activation[40,58]. Consistently, previous studies have shown that FN promotes AKT phosphorylation in a PI3K-dependent manner in fibroblasts lacking FAK or SRC family kinases[59].

ILK was initially described as a kinase, but subsequent studies have suggested that despite containing a kinase-like domain, ILK may function as a pseudokinase, acting as a scaffold for other proteins, including kinases. Although a consensus has not yet been established, most studies agree that ILK induces AKT phosphorylation at S473, a process seemingly dependent on ILK phosphorylation at S343[58,60]. Indeed, we observed an upregulation of pIlk^{S343} in MFS aortas, and that Ilk inhibition prevented Akt phosphorylation and the overactivation of the NO pathway by FN in VSMCs. Whether ILK directly phosphorylates AKT or does so through interactors remains unclear and is beyond the scope of our study.

ILK is essential for vascular development during embryogenesis, with ubiquitous deletion causing embryonic lethality[61], and constitutive SMC-specific deletion causing perinatal lethality and aortic aneurysms due to morphogenetic developmental defects observed as early as E12.5[62,63]. While these findings suggest a protective role of ILK in the vasculature during development, our results strongly suggest a pathogenic contribution of ILK to aortopathy in MFS after birth. Indeed, induced SMC-specific deletion of *Ilk* in young MFS mice prevents aortopathy, and *Ilk* silencing in adult MFS mice regresses aortic disease. Moreover, pharmacological ILK inhibition also regresses aortic disease in adult MFS mice, although this treatment also causes lethality, potentially due to off-target effects of the inhibitor or systemic ILK inhibition. Since Ilk ubiquitous conditional deletion in adult mice did not result in any obvious pathology[64], the lethality induced by the inhibitor is likely caused by off-target effects.

Beyond the *Fbn1*$^{C1041G/+}$ mouse model, we demonstrate that the FN–$\alpha_V\beta_3$–pIlk^{S343}–Nos2 pathway is also overactivated in the aortas of *Fbn1*$^{mgR/mgR}$ MFS mice. Together with its activation in patients carrying a wide range of *FBN1* mutations (Supplementary Table 1), these findings indicate that this mechanism is broadly operative across the MFS patient spectrum.

In summary, we delineate the functional and causal role of FN signaling through integrin $\alpha_V\beta_3$, PI3K, PIP3, PDK1, and ILK in activating AKT and driving NO overactivation in MFS aortas (Fig. 7a). Building on

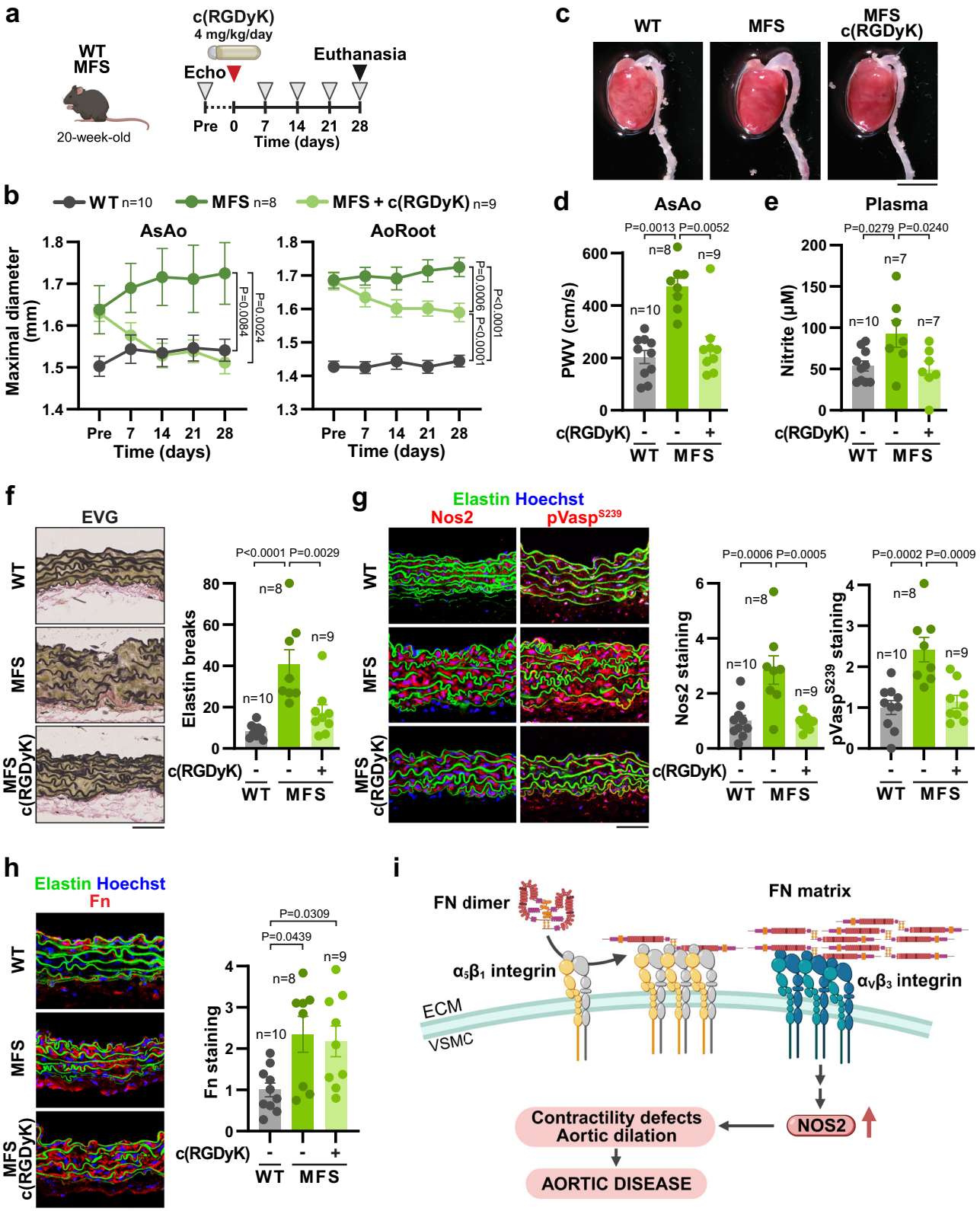

our previous studies, we propose a comprehensive molecular framework linking ECM defects to integrin-mediated signaling, intracellular transducers, and NOS2-derived NO overproduction. This cascade culminates in PKG overactivation, contractility dysregulation, and progressive aortic disease. Our findings identify multiple actionable targets, including FN polymerization, $\alpha_V\beta_3$ integrin, ILK, and PDK1, whose inhibition reverses aortic pathology in MFS mice. The involvement of these mediators in human disease underscores their translational potential and highlights the urgent need to evaluate targeted inhibitors as therapeutic options for MFS patients.

Methods

Ethics

The study complied with all relevant ethical regulations. The use of human aorta samples was approved by the Clinical Research Ethics Committee of Cantabria (ref. 27/2013), and the Ethics Committee of

Fig. 5 | $\alpha_V\beta_3$ integrin-FN interaction drives NO pathway activation and aortic disease in female MFS mice. a Experimental design: female MFS mice were treated 28 days with c(RGDyK). Sham-operated WT and MFS mice served as controls. **b** Maximal AsAo and AoRoot diameters in WT, MFS, and c(RGDyK)-treated MFS mice ($n = 8–10$ as indicated) over time. Data are mean ± s.e.m. **c** Representative images of the gross morphology of thoracic aortas from WT, MFS, and c(RGDyK)-treated MFS mice at the end of treatment. Scale bar, 500 μm. PWV of the AsAo (**d**) and plasma nitrate plus nitrite levels (**e**) in WT, MFS, and c(RGDyK)-treated MFS mice ($n = 7–10$). Data are mean ± s.e.m. **f** Representative EVG staining and quantification of the number of elastin breaks per section in aortas after 28 days of treatment. Scale bar, 50 μm. Data are mean ± s.e.m. Each point represents one mouse ($n = 8–10$ as indicated). Representative images and quantification of Nos2 and $pVasp^{S239}$ (red, **g**) or Fn (red, **h**) immunofluorescence in aortic sections from WT, MFS, and c(RGDyK)-treated MFS mice after 28 days. Elastin autofluorescence (green) and Hoechst-stained nuclei (blue) are shown. Scale bar, 50 μm. Data are shown relative to WT mice as mean ± s.e.m. Each point denotes one mouse ($n = 8–10$ as indicated). **i** Proposed model of integrin-dependent FN dynamics in the MFS aorta. $\alpha_5\beta_1$ integrin promotes FN dimer unfolding and exposure of FN interaction domains, enabling FN multimerization and matrix assembly. The FN matrix subsequently signals through $\alpha_V\beta_3$ integrin to upregulate NOS2 and activate the canonical NO pathway, ultimately driving aortic dysfunction and disease. Statistical significance was assessed by RM two-way ANOVA with Tukey's post-hoc test (**b**), Kruskal–Wallis test with Dunn's multiple comparison test (**d**), or one-way ANOVA with Tukey's post-hoc test (**e**–**h**). **a**, **i** These were created in BioRender. Martin, N. (2026) https://BioRender.com/yi4yh4f. Source data are provided as a Source Data file.

Instituto de Salud Carlos III (CEI PI91_2018-v2-Enmienda_2019 and CEI PI 65_2023) conformed to the principles set out in the WMA Declaration of Helsinki and the Department of Health and Human Services Belmont Report. Informed consent was obtained from all human participants or their families. Clinical data were retrieved while maintaining patient anonymity.

All animal procedures and experiments complied with relevant ethical regulations, were accredited by the CNIC Ethics Committee and the Madrid regional authorities (ref. PROEX 80/16 and PROEX 094.8/21), and conformed to EU Directive 2010/63/EU and Recommendation 2007/526/EC regarding the protection of animals used for experimental and other scientific purposes, enacted in Spanish law under Real Decreto 1201/2005.

Mouse strains

Fbn1$^{C1041G/+}$ MFS mice[65], harboring a mutation in the *Fbn1* gene, were obtained from Jackson Laboratory (JAX mice stock #012885). *Fbn1*$^{mgR/+}$ mice were generously provided by Prof. Sanjay Sinha (Cambridge Stem Cell Institute, Cambridge, United Kingdom). *Myh11-Cre*^{ERT2} mice, expressing Cre recombinase with a modified estrogen receptor binding domain (ERT) under the regulatory sequences of the smooth muscle *Myh11* promoter and inserted into the Y-chromosome[46], were generously provided by Prof. Stefan Offermanns (Max Planck Institute for Heart and Lung Research, Bad Nauheim, Germany).

To specifically delete *Ilk* in SMCs of *Fbn1*$^{C1041G/+}$ mice, we crossed *Fbn1*$^{C1041G/+}$ mice and *Myh11-Cre*^{ERT2} transgenic mice, both on a C57BL/6J background, with *Ilk*$^{flox/flox}$ (*Ilk*$^{f/f}$) mice[45] on a mixed BALB/c and C57BL/6J background. This breeding strategy generated *Fbn1*$^{C1041G/+}$;*Myh11-Cre*^{ERT2};*Ilk*$^{f/f}$ mice and *Fbn1*$^{+/+}$;*Ilk*$^{f/f}$ mice. To maintain this genetic background homogenously, we exclusively crossed animals of this strain. All mouse strains were maintained in hemizygosity for the *Fbn1*$^{C1041G/+}$ mutation and the Cre^{ERT2} transgene, and in homozygosity for the *Ilk*-floxed locus. All mice were genotyped by PCR of genomic DNA obtained from tail samples using the following primers: *Fbn1*$^{C1041G/+}$ mice (5′-CTCATCATTTTTGGCCAGTTG-3′, 5′-GCACTTGATGCACATTCACA-3′); *Ilk*-floxed mice (5′-CCAGGTGGCAGAGGTAAGTA-3′, 5′-CAAGGAATAAGGTGAGCTTCAGAA-3′); *Myh11-Cre*^{ERT2} mice (5′-TGACCCCATCTCTTCACTCC-3′, 5′-AACTCCACGACCACCTCATC-3′, 5′-AGTCCCTCACATCCTCAGGTT-3′).

Animal procedures

Both male and female mice were used in this study. Mouse health was assessed daily for signs of discomfort, weight loss, and changes in behavior, mobility, feeding, or drinking habits. Mice were housed in the CNIC specific pathogen-free animal facility with controlled temperature (20–24°), 45–65% relative humidity, and a 12-h light/dark cycle. Animals were maintained in ventilated rack systems in cages containing wood-chip bedding and adequate nesting material. Environmental enrichment was provided by adding materials and objects inside the cages. All animals had ad libitum access to standard rodent chow and water, and availability was checked daily. Sacrifice of mice was performed by CO_2 inhalation. Gross morphological images of the aortas were acquired using a Leica MZ FLIII stereomicroscope (Leica Microsystems; Wetzlar, Germany) fitted with a Nikon DXM1200F digital camera (Nikon; Tokyo, Japan).

For FN disruption in the aorta of MFS mice, we used FUD (or pUR4), a 64-mer peptide containing the functional upstream domain of *Streptococcus pyogenes* F1 adhesin fused to a 6xHis-tag for tracking (MRGSHHHHHHGSKDQSPLAGESGETEYITEVYGNQQNPVDIDKKLPNETGFSGNMVETEDTKLN)[22]. FUD was produced by Proteogenix (Schiltigheim, France), and its integrity was verified by high-performance liquid chromatography coupled with mass detection (HPLC-MS). Lyophilized FUD was solubilized in sterile PBS and administered by intraperitoneal injection at 25 mg/kg/day for 7 consecutive days. c(RGDyK) (Selleck Chemicals, S7844; Houston, USA) was administered at 4 mg/kg/day for 6 days or 28 days using subcutaneous osmotic minipumps (Alzet Corp, model 2001 or 2004, respectively; Cupertino, USA). PDK1 inhibitor GSK2334470 (Selleck Chemicals, S7087) was administered at 40 mg/kg/day for 6 days using subcutaneous osmotic minipumps. ILK-IN-2 (Ambeed, A623292; Arlington Heights, USA) was administered at 25 mg/kg/day in 90% corn oil and 10% DMSO for 6 consecutive days by intraperitoneal injection. WT and MFS mice injected with vehicle were used as controls for FUD and ILK-IN-2-treated mice. Sham-operated mice were employed as controls for c(RGDyK)- and GSK2334470-treated mice.

For chemical induction of aortic aneurysm, male C57BL/6J mice were administered BAPN and AngII. BAPN was supplied in the drinking water at 1 g/L, whereas AngII was continuously infused at a rate of 1 μg/kg/min via subcutaneously implanted osmotic minipumps (RWD Life Science, model 1002 W; Shenzhen, China). Both treatments were administered concurrently for 13 consecutive days, after which mice were euthanized.

For inducible *Ilk* deletion specifically in SMCs, 4-week-old *Fbn1*$^{C1041G/+}$;*Myh11-Cre*^{ERT2};*Ilk*$^{f/f}$ mice were intraperitoneally injected with 1 mg of TX (Merck, T5648; Darmstadt, Germany) in corn oil daily for 5 consecutive days, generating MFS-ILK$^{SM\text{-}cKO}$ mice. In experiments involving MFS-ILK$^{SM\text{-}cKO}$ mice, *Fbn1*$^{+/+}$;*Ilk*$^{f/f}$ mice injected with TX and *Fbn1*$^{C1041G/+}$;*Myh11-Cre*^{ERT2};*Ilk*$^{f/f}$ littermates mice injected with vehicle were used as WT and MFS controls, respectively.

In vivo ultrasound imaging

Images of the AoRoot, AsAo, and AbAo were obtained from isoflurane-anesthetized mice (1.5% isoflurane) using high-frequency ultrasound with a VEVO 2100 or VEVO F2 echography device (VisualSonics, Toronto, Canada) fitted with a 30 μm axial resolution transducer. Maximal internal aortic diameter was measured at systole using VEVO 2100 software, version 5.6.1 (VisualSonics). Diameter measurements were taken before treatment initiation to determine baseline diameters and at the indicated time points during the experiment.

PWV was measured using a VEVO F2 system (VisualSonics) fitted with a transducer with an axial resolution of 50 μm. Electrocardiogram (ECG) signals were recorded simultaneously with ultrasound images of

https://doi.org/10.1038/s41467-026-74707-4

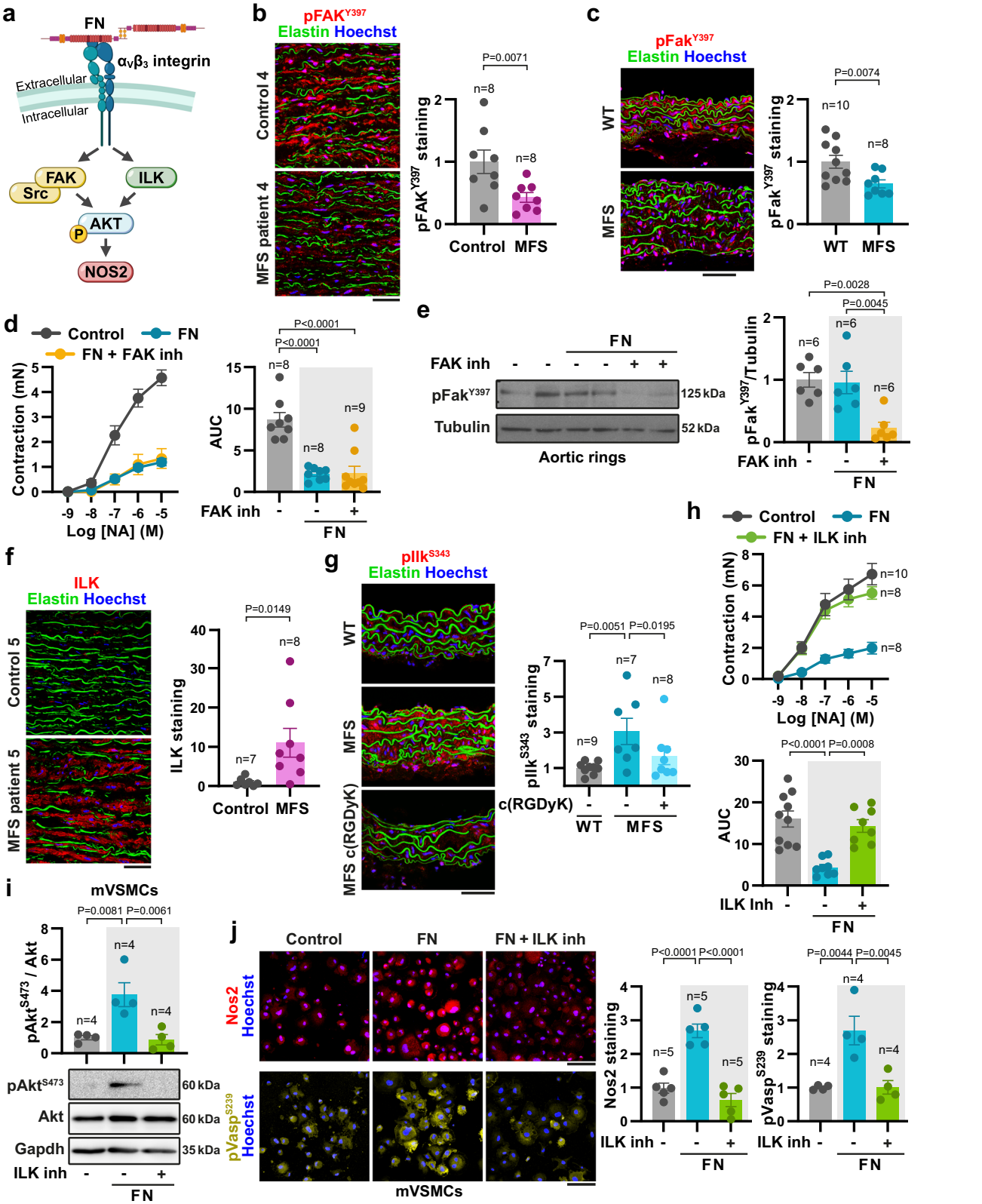

the aortic arch, and blood flow velocity profiles were obtained by Doppler ultrasound at the proximal AsAo and at the distal portion of the aortic arch. PWV was calculated according to equation 1:

$$\mathrm{PWV} = \frac{D}{t_2 - t_1}$$

where PWV is the pulse wave velocity, t_1 and t_2 represent the time intervals between the peak of the R wave in the ECG and the onset of the pulse wave at the proximal AsAo and distal aortic arch, respectively, and D is the distance between the two measurement sites corresponding to t_1 and t_2.

Lentivirus production and infection

MISSION pLKO-puro-based vectors encoded either a non-targeting shRNA (SHC202), the *ITGAV*-targeting shRNA shITGAV (TRCN0000010768) or the *ITGB1*-targeting shRNA shITGB1

Fig. 6 | ILK, but not FAK, is overactivated in MFS and mediates FN-induced contractility impairment. a Schematic representation of candidate kinases linking integrin-mediated FN signaling to AKT activation; created in BioRender. Martin, N. (2026) https://BioRender.com/yi4yh4f. Representative images and quantification of pFAK^{Y397} immunofluorescence (red) in the medial layer of human aortic tissue from 8 controls and 8 MFS patients (**b**) and 10 WT and 8 MFS 20-week-old male mice (**c**). Elastin autofluorescence (green) and Hoechst-stained nuclei (blue) are shown. Scale bar, 50 µm. Data are mean ± s.e.m. Each point represents one individual. **d** Contractile responses to NA and AUC in endothelium-denuded aortas after 6 h incubation with vehicle or FN with or without the FAK inhibitor defactinib. Data are mean ± s.e.m. Each point represents one aorta ($n = 8–9$ as indicated). **e** Representative immunoblots and quantification of pFak^{Y397} in protein extracts from endothelium-denuded aortas from 12-week-old mice incubated with FN ±defactinib for 6 h. Data are shown relative to control as mean ± s.e.m. Each point represents one aorta ($n = 6$ per group). Representative images and quantification of ILK (**f**) or pIlk^{S343} (**g**) immunofluorescence (red) in the medial layer of human aortic tissue from 7 controls and 8 MFS patients (**f**) or in aortas from 9 WT, 7 MFS, and 8 6-day c(RGDyK)-treated MFS male mice (**g**). Elastin autofluorescence (green) and Hoechst-stained nuclei (blue) are shown. Scale bar, 50 µm. Data are mean ± s.e.m. Each point denotes one individual/mouse. **h** Contractile responses to NA and AUC in endothelium-denuded aortas after 6 h incubation with FN ± ILK-IN-2. Data are mean ± s.e.m. Each point represents one aorta ($n = 8–10$ as indicated). Akt activation, Nos2 expression, and pVasp^{S239} levels in mVSMCs seeded on collagen or FN in the absence or presence of ILK-IN-2, assessed by immunoblotting (**i**) and immunofluorescence (**j**). Data are mean ± s.e.m. Each point denotes an independent VSMC batch ($n = 4–5$ as indicated). Statistical significance was assessed by one-sided unpaired Student *t* test (**b**, **c**), one-way ANOVA with Tukey's post-hoc test (**d**, **e**, **g**–**j**), or one-sided Welch *t* test (**f**). Source data are provided as a Source Data file.

(TRCN0000275083). Pseudo-typed lentiviruses were produced by transient calcium phosphate transfection of HEK-293T cells with the shRNA-encoding plasmids. Conditioned medium was harvested, cleared of debris by low-speed centrifugation, and filtered through 0.45-µm filters. For cell transduction, human VSMCs were incubated with the virus-containing medium and 8 µg/mL polybrene for 16 h. Cells were washed and treated 2 days later with 100 nM puromycin for 24 h before stimulating them with FN.

A lentiviral plasmid encoding GFP and shRNA targeting mouse *Ilk* was engineered by cloning a previously validated shRNA against *Ilk* (CCTGAACAAACACTCCGGTAT)[66] or a non-specific shRNA (shScr: CAACAAGATGAAGAGCACCAA), used as a control, into the pH1-DUAL lentiviral vector. Pseudo-typed lentiviruses were produced by transient calcium phosphate transfection of HEK-293T cells with the engineered plasmid. Following medium replacement, cells were harvested after 48 h, and lentiviruses were concentrated from the culture supernatant by ultracentrifugation for 2 h at 122,000 × *g* at 4 °C (Ultraclear Tubes; SW28 rotor, Optima L-100 XP Ultracentrifuge, Beckman; Brea, USA). Lentiviral vectors were suspended in cold sterile PBS, stored at −80 °C to avoid degradation, and titrated by infection of Jurkat cells.

Jurkat cells were seeded in a 96-well plate and infected with the desired lentiviral dilution from 1/10 to 1/100000. After 48 h, cells were centrifuged for 5 min at 4 °C and 650 × g, and resuspended in ice-cold PBS containing propidium iodide (Merck, P4864, 1/1000). Transduction efficiency (% of GFP-expressing cells) and cell death (propidium iodide staining) were assessed by flow cytometry using a Canto 3 L HTS cytometer (BD Biosciences; Franklin Lakes, USA) and the BD FACSDiva Software Version 6.1.3, and analyzed using FlowJo 10.8.1 software.

VSMCs were infected (multiplicity of infection = 10) overnight at 37 °C in growth medium. The medium was then replaced with fresh growth medium, and cells were cultured for 5 additional days before being processed for mRNA expression analysis.

In vivo transduction was performed through intrajugular vein injection of lentiviral particles in 14-week-old mice anesthetized with ketamine and xylazine. A small incision was made to expose the left jugular vein, and 10^9 lentiviral particles (200 µL in PBS) were injected directly into the jugular vein. Transduction and *Ilk* silencing efficiencies were analyzed in aortic samples by GFP and Ilk immunostaining, respectively.

Cell culture

Primary mouse VSMCs were isolated from 6 to 8-week-old male WT C57BL/6J mice based on[67]. Briefly, aortas were dissected, and the adventitia was removed using forceps. The aortic tissue was cut into small rings and digested with 1 mg/ml collagenase type II and 0.5 mg/ml elastase (Worthington, LS004176 and LS002292, respectively; Columbus, USA) until single cells were obtained. Cells were then cultured at 37 °C, 5% CO_2 in Dulbecco's modified Eagle's medium (DMEM, Gibco; Waltham, USA) supplemented with 20% fetal bovine serum (FBS), 2 mM L-glutamine, 100 U/ml penicillin, and 100 µg/ml streptomycin. All experiments were conducted in passage 2 or 3. VSMC identity was confirmed by flow cytometry, showing positive staining for αSMA and absence of CD31 expression (Supplementary Fig. 18). Only VSMCs derived from WT mice were used to specifically assess FN-induced signaling events, thereby avoiding potential confounding effects of pre-activated pathological pathways present in MFS-derived cells. The use of MFS VSMCs could obscure FN-specific responses due to the underlying *Fbn1* mutation.

Human VSMCs derived from umbilical artery (ScienCell, 8030; Carlsbad, USA), generously provided by Dr. Nerea Mendez-Barbero, were cultured at 37 °C, 5% CO_2 in SMC Medium (ScienCell, 1101) supplemented with 10% FBS, 1% SMC growth supplement (ScienCell, 1152) 100 U/ml penicillin, and 100 µg/ml streptomycin. All experiments were performed at passages 9 to 15.

Human aortic SMCs (HAoSMCs) were isolated from the medial layer of a human aorta after careful removal of the endothelium and adventitia. Aortic media fragments (~2 mm^2) were placed in T25 flasks and cultured at 37 °C and 5% CO_2 in human vascular smooth muscle cell basal medium (Gibco, M231500) supplemented with 10% FBS, 5% smooth muscle growth supplement (SMGS; Gibco, S00725), 100 U/ml penicillin, and 100 µg/ml streptomycin. All experiments were performed using cells at passage 3.

Mouse lung endothelial cells (MLECs) were isolated from C57BL/6J mouse lungs and used as positive controls for CD31 expression in VSMC identity analyses (Supplementary Fig. 18). Lung tissue was digested with 0.2% collagenase type I (Gibco, 1700017) for 1 h at 37 °C, followed by negative selection using a rat anti-CD16/CD32 antibody (1/350, BD Biosciences, 553142) and positive selection with a rat anti-ICAM2 antibody (1/350, BD Biosciences, 553325) coupled to Dynabeads Sheep Anti-Rat IgG (Invitrogen, 11035; Waltham, USA). MLECs were cultured at 37 °C and 5% CO_2 on 0.5% gelatin-coated plates in DMEM:F12 medium (Lonza, BE12-719F; Basel, Switzerland) supplemented with endothelial cell growth supplement (1/250, PromoCell, C-30120; Heidelberg, Germany), 20% FBS, 2 mM L-glutamine, 100 U/ml penicillin, and 100 µg/ml streptomycin.

Cell procedures

For in vitro FUD testing and FN matrix immunostaining, VSMCs were seeded on glass coverslips and cultured at 37 °C and 5% CO_2 in DMEM supplemented with 20% FBS, 2 mM L-glutamine, 100 U/mL penicillin, and 100 µg/mL streptomycin. FUD was added to the culture medium at a final concentration of 40 µg/mL. In one experimental set, FUD was added simultaneously with cell seeding and cultures were maintained for 96 h. In a second setting, cells were cultured for 48 h before FUD addition, followed by an additional 48-h incubation (Supplementary Fig. 2a, b). Vehicle-treated cells served as controls. Cells were washed and fixed with 4% paraformaldehyde for 10 min, permeabilized with 0.3% Triton X-100 in PBS for 10 min, and blocked for 1 h with 5% goat serum and 2% BSA in PBS containing 0.01% Triton X-100. FN was

https://doi.org/10.1038/s41467-026-74707-4

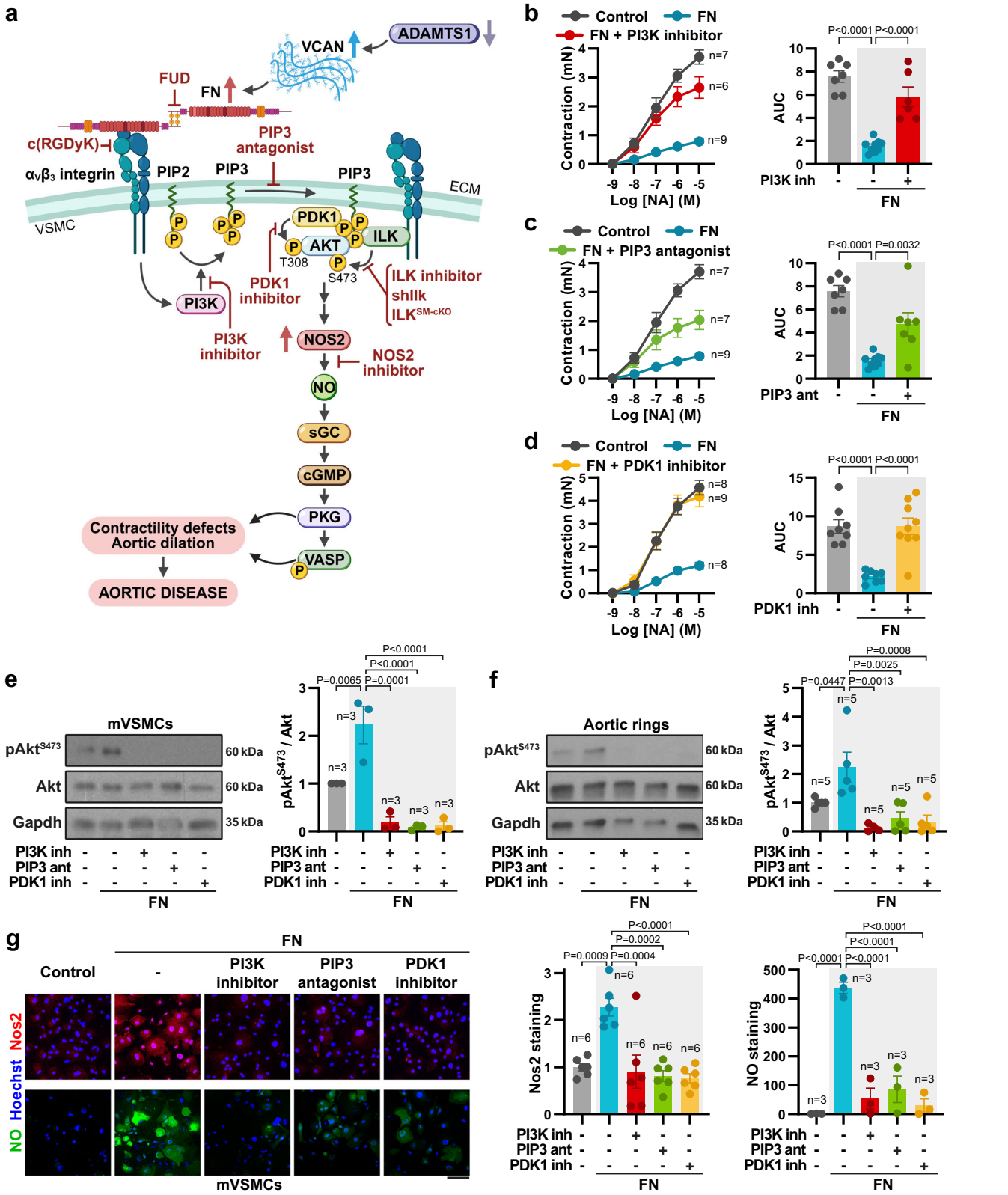

detected using a rabbit polyclonal anti-FN antibody (1/10000; Abcam, ab2033; Cambridge, UK) followed by Alexa Fluor 647-conjugated goat anti-rabbit IgG (1/500; Molecular Probes, Eugene, USA). Antibody specificity was verified by replacing the primary antibody with an unrelated IgG at the same concentration. Nuclei were stained with Hoechst (Merck, B2261), and coverslips were mounted using Citifluor AF4 (Aname, 17973; Quijorna, Spain). Images obtained using unrelated IgG controls are shown in Supplementary Fig. 20.

For adhesion assays, VSMCs were washed and stained with 2.5 μM CellTrace Carboxyfluorescein Succinimidyl Ester (CFSE, Invitrogen, C34554) for 20 min at 37 °C and 5% CO_2 in the dark, followed by incubation with 4% BSA for 5 min to quench excess CFSE. Cells were seeded onto 96-well plates pre-coated for 30 min at 37 °C with 40 μg/mL human FN (Merck, F2006) in the presence or absence of 40 μg/mL FUD, and incubated for 10 min at 37 °C in phenol red–free DMEM under 5% CO_2 in the dark. After incubation, cells were washed twice with PBS to remove

Fig. 7 | FN-$\alpha_V\beta_3$ interaction induces Nos2 via the PI3K-PIP3-ILK-PDK1-AKT cascade. a Schematic representation of the proposed molecular mechanism triggering MFS aortopathy created in BioRender. Martin, N. (2026) https://BioRender.com/yi4yh4f. ADAMTS1 downregulation promotes VCAN accumulation and subsequent FN deposition in MFS aortas, leading to $\alpha_V\beta_3$ integrin-dependent activation of PI3K. PI3K converts PIP2 to PIP3, which recruits PDK1, ILK, and AKT to the plasma membrane. AKT activation by PDK1 and ILK induces NOS2 and NO overproduction, resulting in PKG overactivation, impaired contractility, and medial layer disorganization. Red text indicates experimental interventions used to disrupt this cascade. **b**–**d** Contractile responses to NA and corresponding AUC in endothelium-denuded aortas after 6 h incubation with vehicle or FN. Where indicated, the PI3K inhibitor wortmannin (**b**), the PIP3 antagonist PIT-1 (**c**), or the PDK1 inhibitor GSK2334470 (**d**) were added together with FN. Data are mean ± s.e.m. Each point denotes one aorta ($n = 6$–9 as indicated). Representative immunoblots and quantification of Akt phosphorylation ($pAkt^{S473}$/total Akt) in mVSMCs seeded on collagen or FN for 1 h (**e**), or in aortic rings incubated for 6 h (**f**), in the absence or presence of wortmannin, PIT-1, or GSK2334470. Gapdh served as loading control. Data are shown relative to control as mean ± s.e.m. Each point denotes an independent VSMC batch ($n = 3$ per group) or mouse ($n = 5$ per group). **g** Representative images and quantification of Nos2 immunofluorescence and NO staining in mVSMCs seeded on collagen or FN with or without the indicated inhibitors. Nuclei were stained with Hoechst. Scale bar, 100 μm. Data are mean ± s.e.m. Each point denotes one mVSMC batch ($n = 6$). Statistical significance was assessed by one-way ANOVA with Tukey's post-hoc test (**b**–**g**). Source data are provided as a Source Data file.

cells remaining unattached. Bright-field images were captured before and after washing using a Nikon Eclipse TS100-F microscope coupled with a Nikon Digital Sight DS-2MBW camera (Nikon), and CFSE fluorescence was measured at 492/517 nm (excitation/emission) using a Fluoroskan Ascent microplate fluorometer (Thermo Fisher Scientific; Waltham, USA). Adhesion was expressed as the percentage of fluorescence remaining after washing.

For coating experiments, plates were coated overnight at 37 °C with 40 μg/ml human FN (Merck, F2006) or 40 μg/ml collagen type I (Merck, C8919) as a control. Serum-starved VSMCs or HUASMCs were seeded at ~90% confluence on the FN- or collagen-precoated surfaces, and plates were centrifuged for 5 min at 200 × g and 4 °C to ensure cell adherence. VSMCs were incubated for 1 h at 37 °C and then harvested for protein assays. Longer incubations were not performed in order to preserve viability under serum-free conditions and to selectively capture early signaling events, avoiding confounding stress responses associated with extended serum deprivation.

For cell immunostaining, glass coverslips were placed in 24-well plates and coated overnight at 37 °C with 40 μg/ml of human FN (Merck, F2006) or 40 μg/ml collagen type I (Merck, C8919) plus 10 μg/ml poly-L-lysine (Merck, P2636) as a control. Serum-starved mouse and human VSMCs were seeded at 90% confluence and incubated for 1 h at 37 °C before being fixed with 4% paraformaldehyde for 10 min. Cells were permeabilized with 0.3% Triton X-100 in PBS for 10 min, blocked for 1 h with 5% goat serum plus 2% BSA in PBS containing 0.01% Triton X-100, and incubated with the following primary antibodies: rabbit polyclonal anti-Nos2 (1/100, abcam, ab15323), mouse monoclonal anti-$pVASP^{S239}$ (1/50, Santa Cruz Biotechnology, sc-101439; Dallas, USA), Alexa-Fluor-647-conjugated rabbit monoclonal anti-α_V integrin (1/100, abcam, ab204684), or rat monoclonal anti-β_1 integrin (BD Biosciences, 553715). Specificity was verified by replacing the primary antibody with an unrelated IgG at the same concentration (Invitrogen and Santa Cruz). Polyclonal Alexa-Fluor-647-conjugated goat anti-rabbit or chicken anti-mouse, and Alexa-Fluor-488-conjugated chicken anti-rat (1/500, Molecular Probes) were used as secondary antibodies. Nuclei were stained with Hoechst (Merck, B2261), and coverslips were mounted in Citifluor AF4 mounting medium (Aname, 17973). IgG controls are shown in Supplementary Figs. 19 and 20.

For NO detection, cells were serum-starved for 16 h, seeded on coated coverslips, and incubated for 1 h at 37 °C and 5% CO_2 in phenol red-free DMEM (Gibco, 31-053-02) supplemented with 2 mM L-glutamine, 100 U/ml penicillin, and 100 μg/ml streptomycin. DAF-FM diacetate was added at a final concentration of 7.5 μM for 1 h. Vehicle-treated cells served as controls. Cells were fixed with 4% paraformaldehyde for 10 min, mounted with Hoechst-containing Citifluor AF4, and imaged by confocal microscopy on the same day. Control images are shown in Supplementary Figs. 19 and 20.

Images (1024 ×1024 pixels, 8 bits) were acquired using a Confocal TCS Leica SP5 microscope fitted with a x40 oil-immersion objective (Leica Microsystems) and Leica LAS-AF V2.7.3 acquisition software. Images were processed, analyzed, and quantified with ImageJ software (version 1.52a, NIH, http://rsb.info.nih/ij/) with an intensity threshold set to include only the specific signal. Total fluorescence intensity was corrected for nuclei number and normalized to controls, except for FN matrix immunostaining, which was quantified as percentage of positive area.

In some experiments, the following inhibitors were added to VSMCs 10 min before seeding them on coated plates: the $\alpha_V\beta_3$ integrin inhibitor c(RGDyK) at 1, 10 and 50 μM (Selleck Chemicals, S7844); FAK inhibitor defactinib at 1 μM (MedChemExpress, HY-12289; South Brunswick, USA); SRC inhibitor dasatinib at 1 μM (Selleck Chemicals, S1021); ILK inhibitor ILK-IN-2 at 40 μM (Ambeed, A623292); PDK1 inhibitor GSK2334470 at 1 μM (Selleck Chemicals, S7087); PIP3 inhibitor PIT-1 at 1 μM (Merck, SML0122); PI3K inhibitor wortmannin at 100 nM (Merck, W1628). In experiments with human VSMCs, the mouse monoclonal anti-$\alpha_V\beta_3$ integrin neutralizing antibody (BD Biosciences, 555504) was added at 2 μg/mL to cells 10 min before seeding them on coated plates. Unrelated normal mouse IgG (Santa Cruz Biotechnology, sc-2025) was used as a control at the same concentration.

HEK-293T (CRL-11268) and Jurkat (TIB-152, clone E61) cell lines (ATCC; Manassas, USA) were used for high-titer lentiviral production and titration, respectively, and tested negative for *Mycoplasma*.

Flow Cytometry

To confirm the identity of VSMCs primary cultures, flow cytometry for αSMA (VSMC marker) and CD31 (endothelial cell marker) was performed in MLEC and VSMC cultures. Cells were detached using TrypLE™ (Gibco, 12604013), washed once with PBS, and incubated with FcR Blocking Reagent (1/100, Miltenyi Biotec, 130-059-901; Bergisch Gladbach, Germany) for 45 min. Cells were then washed with 1% BSA in PBS and stained with APC-conjugated rat monoclonal anti-CD31 antibody (1/300, BD Biosciences, 551262) for 45 min. After washing, cells were fixed and permeabilized using a Fixation/Permeabilization Kit (TONBO Biosciences, TNB-0607-KIT; San Diego, USA) for 45 min at 4 °C. αSMA staining was subsequently performed using Cy3-conjugated mouse monoclonal anti-αSMA antibody (1/2000, Sigma-Aldrich, C6198; Saint Louis, USA). Unstained cells were included as negative controls for both markers. Cells were finally centrifuged and resuspended in PBS. The gating strategy is illustrated in Supplementary Fig. 18a.

CD31 fluorescence was analyzed in MLECs, whereas both CD31 and αSMA fluorescence were analyzed in VSMCs using an LSRFortessa HTS flow cytometer (BD Biosciences). Data were processed with FlowJo™ software V10.8.1 (BD Biosciences). A minimum of 12,000 cells per sample were acquired.

PAAm hydrogel preparation

To assess the effect of substrate stiffness on VSMCs, soft and stiff PAAm hydrogels with Young's moduli of 2.8 and 112 kPa, respectively, were prepared based on[68,69]. Briefly, glass coverslips were first functionalized with (3-aminopropyl)triethoxysilane (APTES; Sigma-Aldrich, 281778) to promote adhesion of the PAAm layer. To obtain a uniform polymer coating, the PAAm solution was sandwiched between an

https://doi.org/10.1038/s41467-026-74707-4

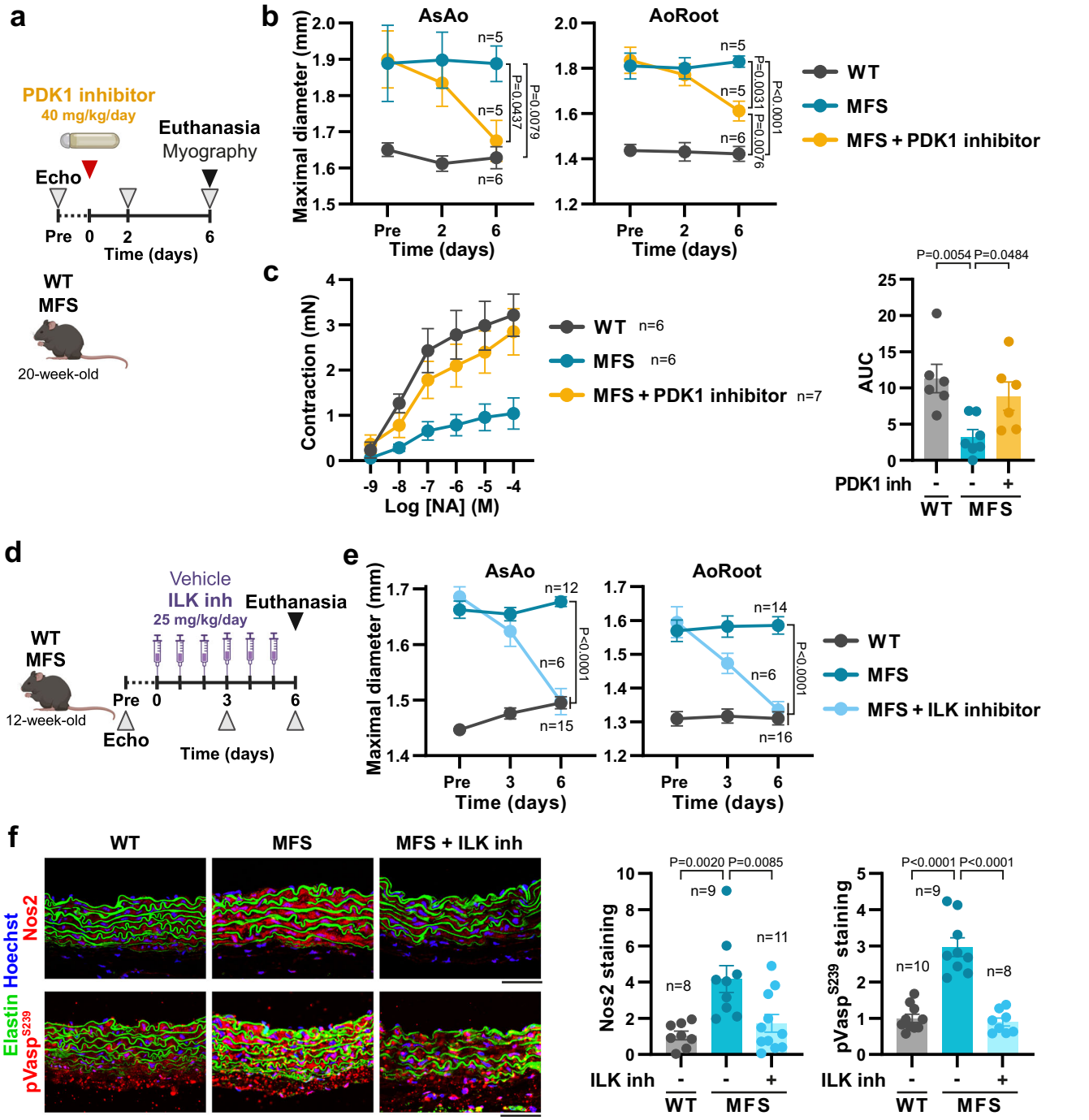

Fig. 8 | Pdk1 and Ilk mediate aortic pathology in MFS through the NO pathway. **a** Experimental design: 20-week-old male MFS mice were treated 6 days with the PDK1 inhibitor GSK2334470. Sham-operated WT and MFS mice were used as controls. **b** Maximal AsAo and AoRoot diameters in WT, MFS, and PDK1 inhibitor-treated MFS mice over time ($n = 5–6$ as indicated). Data are mean ± s.e.m. **c** Contractile responses to NA and corresponding AUC in endothelium-denuded aortas from WT, MFS, and PDK1 inhibitor-treated MFS mice. Each point represents one mouse ($n = 6–7$ as indicated). **d** Experimental design: 12-week-old WT or MFS male mice were treated for 6 days with vehicle (WT and MFS) or the ILK inhibitor ILK-IN-2. **e** Maximal AsAo and AoRoot diameters in WT, MFS, and ILK inhibitor-treated MFS mice over time ($n = 6–16$ as indicated). **f** Representative images and quantification of Nos2 or pVasp^{S239} immunofluorescence (red) in aortic sections from WT, MFS, and ILK-IN-2-treated MFS mice. Elastin autofluorescence (green) and Hoechst-stained nuclei (blue) are shown. Scale bar, 50 µm. Data are shown relative to WT mice as mean ± s.e.m. Each point represents one mouse ($n = 8–11$ as indicated). Statistical significance was assessed by RM two-way ANOVA with Tukey's post-hoc test (**b**,**e**), one-way ANOVA with Dunnett's post-hoc test (c), or one-way ANOVA with Tukey's post-hoc test (**f**). **a**, **d** These were created in BioRender. Martin, N. (2026) https://BioRender.com/yi4yh4f. Source data are provided as a Source Data file.

APTES-treated coverslip and a second coverslip pre-coated with Sigmacote (Sigma-Aldrich, SH25′).

PAAm precursor solutions were prepared by mixing 40% acrylamide (Bio-Rad, 1610140; Hercules, USA) and 2% bis-acrylamide (Bio-Rad, 1610142) stock solutions with molecular biology–grade water (Sigma-Aldrich) at defined ratios to generate gels of different stiffness, following established protocols[68]. Polymerization was initiated by adding 0.5% ammonium persulfate (APS) and 0.15% N,N,N′,N′-tetramethylethylenediamine (TEMED; Thermo Fisher Scientific, 17919). The resulting PAAm hydrogels were activated twice with 0.5 mg/mL Sulfo-

https://doi.org/10.1038/s41467-026-74707-4

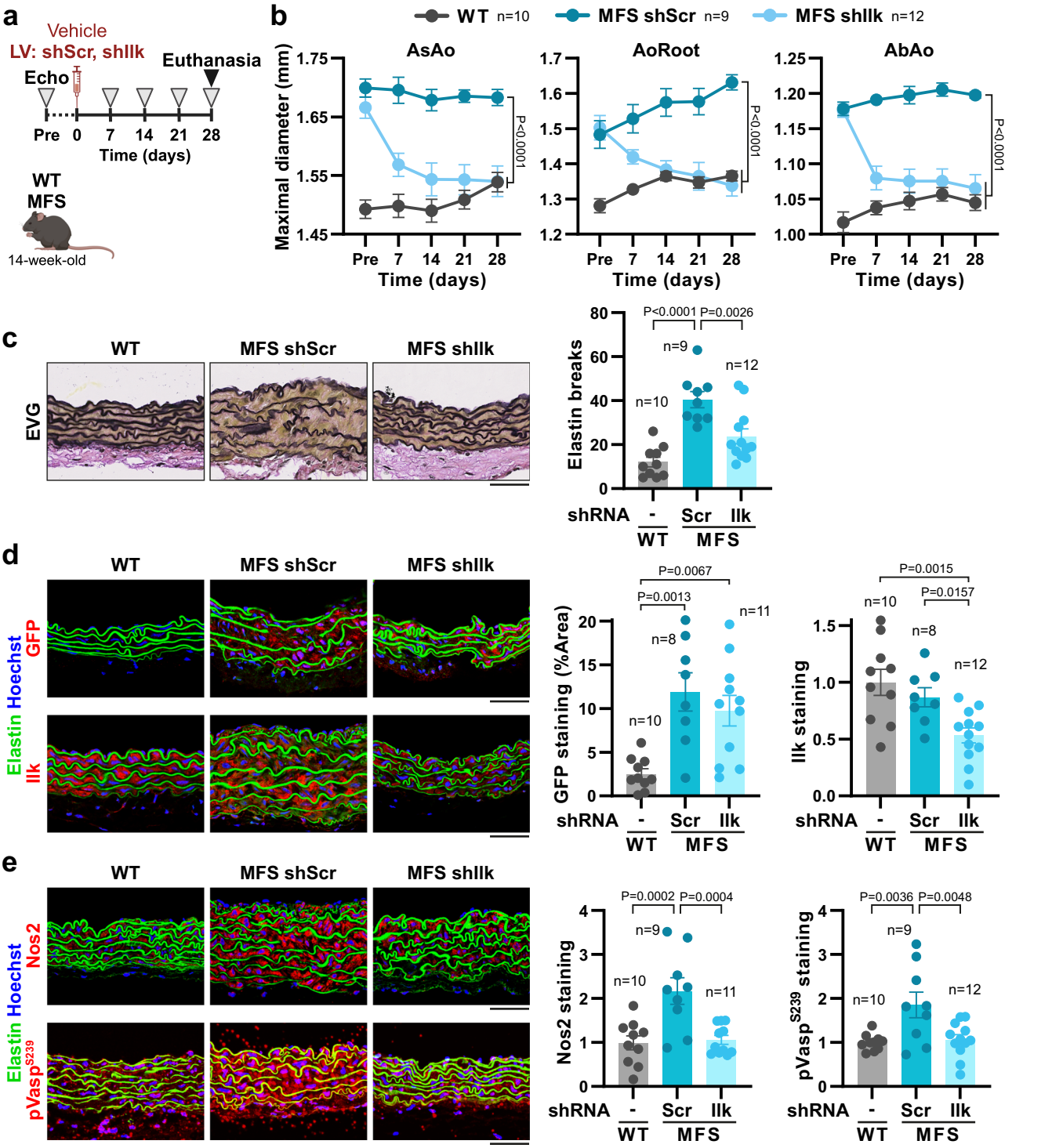

Fig. 9 | Reversion of MFS aortopathy through aortic *Ilk knockdown*.
a Experimental design: 14-week-old WT or MFS male mice were intrajugularly inoculated with vehicle or lentiviral particles encoding *GFP* and a control (shScr) or *Ilk*-specific (shIlk) shRNA. Created in BioRender. Martin, N. (2026) https://BioRender.com/yi4yh4f. **b** Maximal AsAo, AoRoot, and AbAo diameters over time in vehicle-treated WT mice and MFS mice treated with shScr or shIlk lentivirus ($n = 9$–12 as indicated). Data are mean ± s.e.m. **c** Representative EVG staining and quantification of the number of elastin breaks at end point in aortic sections from WT mice and MFS mice treated with shScr or shIlk lentivirus. Scale bar, 50 µm. Data are mean ± s.e.m. Each point denotes one mouse ($n = 9$–12 as indicated). **d** Representative images and quantification of GFP and Ilk immunofluorescence (red) in aortic sections from vehicle-treated WT mice and MFS mice treated with shScr or shIlk lentivirus. Elastin autofluorescence (green) and Hoechst-stained nuclei (blue) are shown. Scale bar, 50 µm. GFP signal is expressed as a percentage of medial area, and Ilk signal relative to WT. Data are mean ± s.e.m. Each point denotes one mouse ($n = 8$–12 as indicated). **e** Representative images and quantification of Nos2 and pVasp^{S239} immunofluorescence (red) in aortic sections from vehicle-treated WT mice and MFS mice treated with shScr or shILK. Elastin autofluorescence (green) and Hoechst-stained nuclei (blue) are shown. Scale bar, 50 µm. Data are shown relative to WT as mean ± s.e.m. Each point denotes one mouse ($n = 9$–11 as indicated). Statistical significance was assessed by RM two-way ANOVA with Tukey's post-hoc test (**b**) or one-way ANOVA with Tukey's post-hoc test (**c**–**e**). Source data are provided as a Source Data file.

https://doi.org/10.1038/s41467-026-74707-4

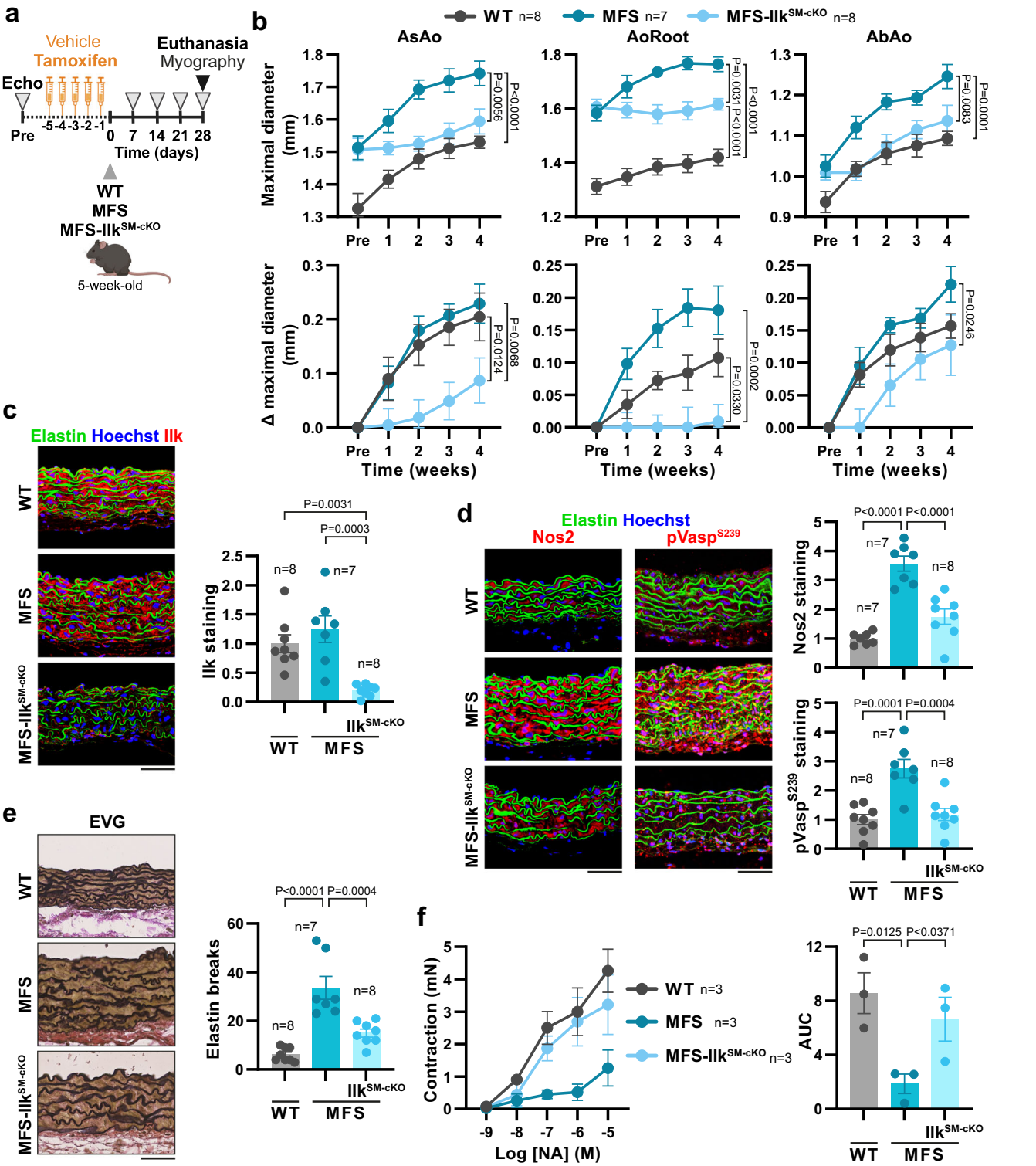

Fig. 10 | Smooth muscle Ilk mediates MFS aortopathy. a Experimental design: 4-week-old *Fbn1*$^{+/+}$;*Ilk*$^{f/f}$ male mice (WT) or *Ilk*-floxed MFS male mice (*Fbn1*$^{C1041G/+}$;*Myh11-Cre*^{ERT2};*Ilk*$^{f/f}$) were intraperitoneally injected for 5 consecutive days with vehicle (*Ilk*-floxed MFS) or tamoxifen (WT and *Ilk*-floxed MFS) to induce smooth muscle-specific *Ilk* deletion (MFS-ILK$^{SM\text{-}cKO}$). Created in BioRender. Martin, N. (2026) https://BioRender.com/yi4yh4f. **b** Maximal AsAo, AoRoot, and AbAo diameters and relative diameter increase from baseline (Pre) in WT, MFS, and MFS-ILK$^{SM\text{-}cKO}$ mice ($n = 7–8$ as indicated). Data are mean ± s.e.m. Representative images and quantification of Ilk (**c**) and Nos2 or pVasp^{S239} (**d**) immunofluorescence (red) in aortic sections from WT, MFS, and MFS-ILK$^{SM\text{-}cKO}$ mice. Elastin autofluorescence (green) and Hoechst-stained nuclei (blue) are shown. Scale bar, 50 µm. Data are expressed relative to WT as mean ± s.e.m. Each point denotes one mouse ($n = 7–8$ as indicated). **e** Representative EVG staining and quantification of elastin breaks in aortic sections from WT, MFS, and MFS-ILK$^{SM\text{-}cKO}$ mice at endpoint. Scale bar, 50 µm. Data represent the number of elastin breaks per section and are shown as mean ± s.e.m. Each point denotes one mouse ($n = 7–8$ as indicated). **f** Contractile responses to NA and corresponding AUC in endothelium-denuded aortas from WT, MFS, and MFS-ILK$^{SM\text{-}cKO}$ mice. Each point represents one mouse ($n = 3$). Statistical significance was assessed by RM two-way ANOVA with Tukey's post-hoc test (**b**) or one-way ANOVA with Tukey's post-hoc test (**c**–**f**). Source data are provided as a Source Data file.

SANPAH (Sigma-Aldrich, 80332) for 6 min at room temperature and subsequently coated with fibronectin (40 μg/mL; Sigma-Aldrich, F2006) for 1 h at 37 °C. Hydrogels were then washed three times with PBS and used immediately.

Atomic force microscopy

Aortic rings (2 mm in length) were excised from the descending thoracic aorta of 20-week-old female WT and MFS mice. The adventitia and endothelium were carefully removed, and aortic rings were incubated overnight in FBS-free DMEM supplemented with 40 μg/mL FUD (or vehicle as control).

AFM measurements were performed using a JPK NanoWizard 4 system (Bruker, Billerica, USA) controlled by JPK SPM Software and integrated with an inverted Axio Observer D1 optical microscope (Zeiss, Oberkochen, Germany). Measurements were performed using CP-qp-CONT-SiO-C-5 cantilevers (NanoAndMore, Wetzlar, Germany) bearing 6.62 μm-diameter colloidal probes and a nominal spring constant of 0.1 N/m. Cantilevers were calibrated prior to measurements using the thermal noise method[70].

Aortic rings were opened longitudinally and mounted endothelium-side up on glass microscope slides using Histoacryl tissue adhesive (B. Braun, Melsungen, Germany) and immersed in PBS at room temperature. Force–distance curves were acquired in contact mode over at least four distinct $10 \times 10\ \mu m^2$ regions per sample, separated by several micrometers, with 400–500 curves collected per tissue. Approach–retract cycles were performed at a tip velocity of 10 μm/s with a maximum indentation amplitude of 3 μm, a 5 nN setpoint force, and 0.1 s contact time.

Young's modulus was calculated using JPK Data Analysis software by fitting the approach segment of the FD curves to the Hertz model for spherical indenters according to equation 2:

$$F = \frac{4}{3}\frac{E}{1-\upsilon^2}\sqrt{R\delta^3}$$

where F is the applied force, R the probe radius, δ the indentation depth, υ the Poisson's ratio (0.5, assuming incompressibility), and E the Young's modulus.

Myography

Aortic rings (2 mm in length) were excised from the descending thoracic aorta of 8- to 12-week-old mice. In some experiments, aortic rings from WT C57BL/6 J male mice were incubated in FBS-free DMEM with 40 μg/mL FN (Sigma-Aldrich, F2006) or PBS (control) for 6 h at 37 °C and 5% CO_2. When indicated, the following inhibitors were added to the aortic rings along with FN: 40 μg/mL FUD, 10 μg/mL neutralizing antibodies against α_V integrin (Invitrogen, 14-0512-82) or β_1 integrin (BD Biosciences, 553715), 100 μM c(RGDyK); 1 μM defactinib; 1 μM dasatinib; 1 μM ILK-IN-2; 1 μM GSK2334470; 2.5 μM PIT-1; or 100 nM wortmannin. In other experiments, aortic rings from the descending thoracic aorta of WT, MFS, MFS-Ilk$^{SM\text{-}cKO}$, and GSK2334470-treated MFS male mice were used directly after excision. The endothelium was removed, and the rings were placed on a wire myograph (model 610 M, Danish Myo Technology; Hinnerup, Denmark) for isometric tension measurements. The organ chamber was filled with Krebs solution (118 mM NaCl, 4.75 mM KCl, 25 mM $NaHCO_3$, 1.2 mM $MgSO_4$, 2 mM $CaCl_2$, 1.2 mM KH_2PO_4 and 11 mM glucose), heated at 37 °C and constantly infused with carbogen (5% CO_2 and 95% O_2, pH ~7.4). Aortic rings were stretched to tension of 5 mN and equilibrated for 30 min. Tension characteristics were recorded using myograph software LabChart (AD Instruments, Dunedin, New Zeland). Endothelium-denuded aortic rings were initially stimulated with 80 mM KCl to confirm responsiveness. This was followed by the construction of L-noradrenaline (NA, Merck, A9512) concentration-response curves (1 nM to 10 μM). When indicated, the NOS2-specific inhibitor 1400 W (10 μM, Tebubio, T3491; Le Perray-en-Yvelines, France) was added to the chamber after the initial NA stimulation, incubated for 30 min, and the NA concentration-response curve was repeated. Vasoconstriction measurements are presented as the force (mN) exerted by the rings. Some myography experiments were performed simultaneously with different inhibitors; hence, some data are repeated in different panels with different inhibitors. Specifically, control and FN data are repeated in Figs. 2d, 7b, c, and Supplementary Fig. 9c. Control + NOS2 inhibitor and FN + NOS2 inhibitor data are repeated in Fig. 2d and Supplementary Fig. 9c. Control and FN data are repeated in Figs. 6d, 7d, and Supplementary Fig. 12b.

For immunofluorescence and immunoblot analyses, aortic rings were incubated for 6 h as as described above and processed immediately thereafter according to the procedures detailed in the *Histology* and *Immunoblot analysis* sections.

NO levels in plasma

Plasma NO levels were quantified as the sum of nitrite and nitrate using the Nitric Oxide Assay Kit (Sigma-Aldrich, MAK454) and measured by absorbance with a Benchmark Plus microplate reader (Bio-Rad). Mouse blood was collected by cardiac puncture following euthanasia by CO_2 inhalation, transferred to EDTA-coated tubes, and centrifuged at 13,000 × g for 15 min at 4 °C to obtain plasma. Plasma samples were deproteinized using $ZnSO_4$ and NaOH, followed by enzymatic reduction of nitrate to nitrite. Nitrite concentrations were then determined using the Griess reaction, according to the manufacturer's instructions.

Histology

After sacrifice by CO_2 inhalation, mouse aortas were perfused with saline solution, fixed overnight at 4 °C in 10% formalin, and embedded in paraffin. For OCT samples, aortas were fresh-frozen immediately after sacrifice. Paraffin-embedded aortic cross sections (5 μm) were stained with Elastin Van Gieson (EVG) stain (Merck). Images were acquired using a Zeiss Axio Scan.Z1 scanner and processed using the NDP.view 2 V2.7.39+ software. Elastic lamina fragmentation (defined as disruptions in elastic fibers) was determined from EVG staining, in 2 complete aortic cross sections per sample. The number of mice per group is indicated in the figure legends.

For immunofluorescence assays, OCT samples were thawed and fixed for 15 min with 4% PFA. Paraffin-embedded murine or human aortic cross sections were deparaffinized, rehydrated and boiled for 3 min in citrate buffer (10 mM sodium citrate, 0.05% Tween 20, pH 6.0) for antigen retrieval. Aortic sections were permeabilized with 0.3% Triton X-100 in PBS for 15 min, blocked for 1 h with 5% goat serum, 5% horse serum, and 2% BSA in PBS containing 0.01% Triton X-100, and incubated with the following antibodies: mouse monoclonal anti-pVASP^{S239} (paraffin-embedded mouse samples, 1/50, Santa Cruz Biotechnology, sc-101439), Alexa-Fluor-647-conjugated rabbit monoclonal anti-α_V integrin (paraffin-embedded mouse and human samples, 1/100, abcam, ab204684), armenian hamster monoclonal anti-β_3 integrin (OCT-embedded mouse samples, 1/200, Invitrogen, 16-0611-82), rabbit polyclonal anti-$\alpha_V\beta_3$ integrin (OCT-embedded mouse samples and paraffin-embedded human samples, 1/100, Bioss Antibodies, bs-1310R; Woburn, USA), rabbit polyclonal anti-pFAK^{Y397} (paraffin-embedded mouse and human samples, 1/100, Cell Signaling Technology, CST #3283; Danvers, USA) or rabbit monoclonal anti-ILK (1/500 for paraffin-embedded mouse samples; 1/1000 for paraffin-embedded human samples; Cell Signaling Technologies, CST #3856), or rabbit polyclonal anti-pILK^{S343} (OCT-embedded mouse samples, 1/100, Abcepta, AP3679a; San Diego, USA). For GFP staining, OCT aortic sections were blocked with 10% goat serum, 10% horse serum, and 4% BSA in PBS containing 0.01% Triton X-100, and incubated with chicken polyclonal anti-GFP (1/500, abcam, ab13970).

For FN, Collagen-I, and FUD staining, aortic samples were fixed for 10 min in acetone, blocked for 1 h with 5% goat serum and 2% BSA in

PBS, and incubated with the following antibodies: rabbit polyclonal anti-FN (1/10000 for OCT-embedded mouse samples; 1/100 for paraffin-embedded human samples, abcam, ab2033), rabbit polyclonal anti-Collagen Type I (OCT-embedded mouse samples, 1/100, Merck, AB765P), and mouse monoclonal anti-6x-His-tag (OCT-embedded mouse samples, 1/100, Invitrogen, MA1-21315).

For Nos2 immunostaining, paraffin samples were deparaffinized, boiled for 3 min in EDTA buffer (10 mM Tris base, 1 mM EDTA, 0.5% Tween 20, pH 9.0), and blocked for 1 h with 5% goat serum and 2% BSA in PBS containing 0.01% Triton X-100. Aortic sections were then incubated with rabbit polyclonal anti-Nos2 (1/100, abcam, ab15323).

For Vcan staining, deparaffined sections were digested with 0.2 UI/ml chondroitinase ABC (Sigma-Aldrich, C3667) and 0.2 UI/ml heparinase (Sigma-Aldrich, H8891) in 20 mM Tris HCl pH8, 50 mM CaCl2, 50 mM sodium acetate for 30 min at 37 °C to remove glycosaminoglycans, blocked with 5% goat serum plus 2% BSA in PBS containing 0.05% Triton X-100, and incubated with rabbit polyclonal anti-Vcan antibody (1/100, Merck, AB1033).

The specificity of antibodies was confirmed by replacing the primary antibody with an unrelated IgG of the same species and concentration: rabbit (Invitrogen), mouse (Santa Cruz) or armenian hamster (Invitrogen); or IgY from chicken (Exalpha Biological, Shirley, USA). Negative control images are shown in Supplementary Figs. 19 and 20. The following Alexa-Fluor-647-conjugated secondary antibodies were used: goat anti-rabbit or chicken anti-mouse (1/500, Molecular Probes), goat anti-armenian hamster (1/500, Jackson ImmunoResearch, Ely, UK) or goat anti-chicken (1/500, Invitrogen). Nuclei were stained with Hoechst (Merck, B2261), and aortic sections were mounted in Citifluor AF4 mounting medium (Aname, 17973). Images (1024 ×1024 pixels, 8 bits) were acquired with an x40 oil-immersion objective using Confocal TCS Leica SP5 microscope (Leica Microsystems) and Leica LAS-AF V2.7.3 acquisition software.

Images were processed, analyzed, and quantified using Fiji ImageJ software (version 1.54p) by defining a region of interest (ROI) and setting intensity thresholds to include only specific signals from the tunica media. Total intensity was corrected for medial aortic area and normalized to control mouse or human samples. For GFP and 6x-His tag detection, the immunofluorescence signal was quantified as a percentage of the positive medial aortic area. Hyperplasia was quantified by counting Hoechst-stained nuclei in three sections and expressed as total number and as a percentage of stained area relative to the medial area.

For FN localization relative to elastin, the elastin channel was thresholded and digitally dilated to create a 6-μm-wide line around elastin sheets (ROI). FN intensity within this ROI was measured and normalized to that of control mice.

For visualization of ECM, OCT sections were thawed, fixed in cold acetone for 10 min, washed with PBS, and imaged by SHG using a STELLARIS 8 DIVE multiphoton microscope (Leica Microsystems). Acquired images were reconstructed in three dimensions using Imaris Viewer V10.2.0 (Oxford Instruments; Abingdon, UK).

Immunoblot analysis

Mouse aortas were isolated, and perivascular tissue and adventitia were removed using forceps. The tissue was frozen in liquid nitrogen and then homogenized using a MagNA Lyser (Roche; Basel, Switzerland). To verify the inhibitory effects of defactinib and dasatinib (FAK and SRC inhibitors, respectively), aortic rings were incubated for 6 h with PBS (as control), FN (40 μg/mL) or FN plus 1 μM defactinib, or FN plus 1 μM dasatinib. These aortic rings were then frozen in liquid nitrogen and homogenized using the MagNA Lyser. Cultured VSMCs were washed with ice-cold PBS prior to lysis.

Aortic tissue, aortic rings, VSMCs and HUASMCs were lysed in RIPA buffer (150 mM NaCl, 50 mM Tris HCl pH8, 1% NP-40, 0.1% SDS, and 0.5% sodium deoxycholate) supplemented with protease and phosphatase inhibitors (100 μM benzamidin, 1 μg/ml leupeptin, 1 μg/ml pepstatin, 1 μg/ml aprotinin, 1 μM dithiothreitol, 1 mM PMSF, 1 mM Na_3VO_4, 0.5 mM NaF, and 1 mM EDTA).

Proteins extracts were separated under reducing conditions on SDS–polyacrylamide gels, transferred to nitrocellulose membranes, and detected using the following antibodies: rabbit monoclonal anti-pAKT^{S473} (1/1000, Cell Signaling Technologies, CST #4060), HRP-conjugated rabbit monoclonal anti-AKT (1/1000, Cell Signaling Technologies, CST #8596), mouse monoclonal anti-GAPDH (1/2000, abcam, ab8245), rabbit monoclonal anti-FAK (1/1000, Cell Signaling Technologies, CST #13009), rabbit polyclonal anti-pFAK^{Y397} (1/1000, Cell Signaling Technologies, CST #3283), rabbit polyclonal anti-pFAK$^{Y576/577}$ (1/4000, Cell Signaling Technologies, CST #3281), mouse monoclonal anti-α-tubulin (1/40000, Merck, T6074).

For pAKT/AKT or pFAK/FAK immunoblots, pAKT or pFAK were detected first. Membranes were then incubated for 3 h with 1% sodium azide in PBS to eliminate HRP activity, washed, and incubated with HRP-conjugated anti-AKT or stripped and incubated with anti-FAK

Bound antibodies were detected using enhanced chemiluminescence (ECL) detection reagent (Millipore; Burlington, USA) and quantified using Fiji ImageJ software (version 1.54p). All uncropped and unprocessed blots from the Main Figures are presented as a Source Data file. All uncropped and unprocessed blots from the Supplementary Figs. are presented in Supplementary Fig. 21.

Real-time and quantitative PCR

Total RNA was isolated from mouse aortas (after removing perivascular and adventitial tissues) and VSMCs using TRIzol (Invitrogen). Total RNA (2 μg) was reverse transcribed at 37 °C for 50 min in a 20 μL reaction mix containing 200 U Moloney murine leukemia virus reverse transcriptase (Promega), 100 ng random primers, and 40U RNase inhibitor (Invitrogen). The resulting cDNA was analyzed by real-time quantitative PCR (qPCR) using a QuantStudio 5 qPCR system (Applied Biosystems) and SYBR master mix (Promega). The following primers, acquired from Merck, were used: *Fn1* (CGAGGTGACAGAGACCACAA, CTGGAGTCAAGCCAGACACA), *Gfp* (CCTGAGCAAAGACCCCAAC, CTTGTACAGCTCGTCCATGC), *Ilk* (ACGACATTTTCACTCAGTG, TCATCCCCACGATTCATCAC), and *Gapdh* (TGACGTGCCGCCTGGAGAAA, AGTGTAGCCCAAGATGCCCTTCA). qPCR reactions were performed in triplicate. Probe specificity was assessed with a post-amplification melting-curve analysis, ensuring only one melting-temperature (Tm) peak per reaction. The relative amount of target mRNA in each sample was estimated using the $2^{-\Delta\Delta CT}$ method and normalized to the expression of *Gapdh*. Data were analyzed with QuantStudio Design & Analysis Software version 1.5.2 and further processed in Microsoft Excel 2019, version 16.0.10404.20013.

Human samples

Aorta samples were obtained during elective AoRoot replacement in patients with MFS from the Hospital Universitari Vall d'Hebron Biobank (National Registry of Biobanks B.000018, PT20/00107). Specific genetic mutations of each MFS patient are indicated in Supplementary Table 1. Control aortas were anonymously obtained from age- and sex-matched multiorgan transplant donors. During heart preparation for transplantation, excess AsAo tissue was trimmed and harvested for the study. Control and MFS samples from male and female individuals (aged 27 to 79 years) were immediately fixed, kept at room temperature for 48 h, and then embedded in paraffin.

Proteomics

High-throughput quantitative proteomics were performed by multiplexed isobaric labeling in AsAo tissue from 12-week-old C57BL/6J MFS mice and WT littermates as controls. There are n = 6 biological replicates per group, and each biological replicate is the pool of two biological samples (a total of 24 animals). Each TMT 10-plex batch contained biological replicates from each experimental condition and

an internal standard for TMT comparison. Two channels were reserved for internal reference standards created by pooling the WT peptide samples. Proteins were extracted from AsAo (50 μg per pool) by tissue homogenization with ceramic beads (MagNa Lyser Green Beads, Roche, Germany) in extraction buffer (100 mM Tris-HCl pH 7.4, 1 mM EDTA, 4% SDS). Proteins were denatured by boiling for 5 min and subjected to filter-aided digestion (Nanosep Centrifugal Devices with Omega Membrane-10K, PALL; New York, USA)[71]. Briefly, urea was added to each sample to reduce SDS concentration to 0.06%. Samples were transferred to the filter and centrifuged at 14,000 × *g* for 10 min. Cys residues were blocked with 50 mM iodoacetamide for 1 h at room temperature in the dark. Samples were washed three times with 100 μl 50 mM ammonium bicarbonate pH 8.8, and proteins digested with trypsin (1:30 trypsin:protein, Promega) overnight at 37 °C. After protein digestion, peptides were eluted from the filter in two steps, first with 40 μl 0.5 M ammonium bicarbonate and then with 50 μl 0.5 M NaCl. Peptides were acidified with trifluoroacetic acid to a final concentration of 1%, desalted on C18 Oasis HLB cartridges (Waters; Milford, USA), and vacuum-dried. Peptides were TMT-labeled according to the manufacturer's instructions and desalted on OASIS extraction cartridges. Peptides were separated into five fractions (Fr1, 12.5%; Fr2, 15%; Fr3, 17.5%; Fr4, 20%; and Fr5, 50%) using the high pH reversed-phase peptide fractionation kit (Thermo Fisher Scientific), and dried-down before MS analysis. Labeled peptide samples were analyzed using a Proxeon Easy nano-flow HPLC system (Thermo Fisher Scientific) coupled via a nanoelectrospray ion source (Thermo Fisher Scientific) to a Q-Exactive HF mass spectrometer (Thermo Fisher Scientific). A C18-based reverse phase separation was used, with a 2-cm trap column and a 50-cm analytical column (75 μm I.D, 2 μm particle size, Acclaim PepMap RSLC, 100 C18; Thermo Fisher Scientific). Peptides were loaded in buffer A (0.1% formic acid in water (v/v)) and eluted with an acetonitrile gradient consisting of 0–30% buffer B (80% acetonitrile, 0.1% formic acid) for 300 min and 50–90% B for 3 min at a flow rate of 200 nl/min. Mass spectra were acquired in a data-dependent manner, with an automatic switch between MS and MS/MS using a top-15 acquisition method with dynamic exclusion. MS spectra were acquired with a mass range of 400–1500 m/z and 120,000 FT resolution. HCD fragmentation was performed at 30% normalized collision energy, and MS/MS spectra were analyzed at 30,000 resolution in the orbitrap. Proteins were identified with the SEQUEST HT algorithm integrated in Proteome Discoverer 2.1 (Thermo Fisher Scientific) against a mouse database. The mouse reference proteome database (UniProtKB/Swiss-Prot and TrEMBL December_2016) was supplemented with 116 CRAP proteins (Global Proteome Machine) (50915 sequences) and was concatenated with the inverted database constructed from the same target databases (101830 sequences in total) using DecoyPYrat[72]. For database searching, parameters were selected as follows: trypsin digestion with two maximum missed cleavage sites, precursor mass tolerance of 2 Da, and a fragment mass tolerance of 30 ppm. Met oxidation (15.994915 Da), Trp-nitration (44.985078 Da), and Tyr nitration (44.985078 Da) were set as variable modifications. Fixed modifications were 57.021464 Da in Cys and 229.162932 Da in Lys and in the peptide N-terminal position. The false discovery rate (FDR) was calculated based on the search of results against the corresponding decoy database using the refined method[73] with an additional filter for precursor mass tolerance of 15 ppm[74] and estimation of the corrected Xcorr. An FDR of 1% was used as the criterion for peptide identification[75].

Quantitative information from TMT reporter intensities was integrated from the spectrum level to the peptide level and then to the protein level based on the WSPP model[76] using the GIA integration algorithm[77]. Quantitative results were expressed as log2(A_i/*IS*), where A_i is the intensity of the TMT reporter of the corresponding sample *i* and *IS* is the mean intensity of the TMT reporters from the internal standard. Relative changes in protein abundance (log2-ratios) were expressed in standardized units (Zq)[76] and statistical analysis was performed as described[78,79].

The mass spectrometry raw data have been deposited to the ProteomeXchange Consortium via the PRIDE[80] partner repository with the dataset identifier PXD077940 and are also publicly available in the Peptide Atlas repository (http://www.peptideatlas.org/PASS/PASS01528).

Statistics and reproducibility

Statistical analysis was performed with GraphPad Prism 9.5.1. The ROUT method was first used to identify and exclude outliers. Data normality was assessed using the D'Agostino-Pearson and Shapiro–Wilk normality tests, and appropriate tests were chosen according to the data distribution. Differences were analyzed using the Student or the Welch *t* test (depending on variance equality as per the F-test); one-way, two-way, or repeated-measures two-way analysis of variance (ANOVA) with the Tukey post hoc test (for experiments with ≥3 groups); the Kruskal–Wallis test with Dunn's multiple comparison test, or the Welch ANOVA with the Dunnett multiple comparisons test, as appropriate. Survival differences were analyzed using the log-rank test. Statistical significance is indicated in each figure.

Sample size was determined empirically based on prior experimental experience and knowledge of variability in the assays used. Sample sizes were selected to be consistent with those commonly used in the field for similar mechanistic studies and based on previously published work using comparable models. In addition, the experimental design relied on multiple complementary approaches (in vivo, ex vivo, and in vitro), which consistently showed robust and reproducible effects, supporting the adequacy of the sample sizes used. The exact number of animals or biological replicates included in each experiment is indicated in the corresponding figure panels and figure legends. All experiments were performed with at least three biological replicates, and all replication attempts were successful. No randomization was performed to allocate animals into experimental groups, and investigators were not blinded to group allocation during in vivo experiments. Experimental groups were balanced in terms of animal age, weight, and aortic basal diameter. Animals were genotyped before experiments, caged together, and treated in the same manner.

Reporting summary

Further information on research design is available in the Nature Portfolio Reporting Summary linked to this article.

Data availability

The mass spectrometry raw data that support the findings of this study have been deposited to the ProteomeXchange Consortium via the PRIDE [80] partner repository with the dataset identifier PXD077940 and are also publicly available in the Peptide Atlas repository (http://www.peptideatlas.org/PASS/PASS01528). Source data are provided with this paper.

References

1. Lindsay, M. E. & Dietz, H. C. Lessons on the pathogenesis of aneurysm from heritable conditions. *Nature* **473**, 308–316 (2011).
2. Toral, M., de la Fuente-Alonso, A., Campanero, M. R. & Redondo, J. M. The NO signalling pathway in aortic aneurysm and dissection. *Br. J. Pharm.* **179**, 1287–1303 (2022).
3. Elefteriades, J. A. & Farkas, E. A. Thoracic aortic aneurysm clinically pertinent controversies and uncertainties. *J. Am. Coll. Cardiol.* **55**, 841–857 (2010).
4. Berger, T. et al. Thoracic aortic aneurysm. *Nat. Rev. Dis. Prim.* **11**, 34 (2025).
5. Dietz, H. C. et al. Marfan syndrome caused by a recurrent de novo missense mutation in the fibrillin gene. *Nature* **352**, 337–339 (1991).

6. Judge, D. P. & Dietz, H. C. Marfan's syndrome. *Lancet* **366**, 1965–1976 (2005).
7. Loeys, B. L. et al. The revised Ghent nosology for the Marfan syndrome. *J. Med. Genet.* **47**, 476–485 (2010).
8. Michel, J. B., Jondeau, G. & Milewicz, D. M. From genetics to response to injury: vascular smooth muscle cells in aneurysms and dissections of the ascending aorta. *Cardiovasc. Res.* **114**, 578–589 (2018).
9. Mazzolai, L. et al. 2024 ESC Guidelines for the management of peripheral arterial and aortic diseases. *Eur. Heart J.* **45**, 3538–3700 (2024).
10. Bossone, E. & Eagle, K. A. Epidemiology and management of aortic disease: aortic aneurysms and acute aortic syndromes. *Nat. Rev. Cardiol.* **18**, 331–348 (2021).
11. Selamet Tierney, E. S. et al. Beta-blocker therapy does not alter the rate of aortic root dilation in pediatric patients with Marfan syndrome. *J. Pediatr.* **150**, 77–82 (2007).
12. Yetman, A. T., Bornemeier, R. A. & McCrindle, B. W. Usefulness of enalapril versus propranolol or atenolol for prevention of aortic dilation in patients with the Marfan syndrome. *Am. J. Cardiol.* **95**, 1125–1127 (2005).
13. Ruiz-Rodríguez, M. J. et al. Versican accumulation drives Nos2 induction and aortic disease in Marfan syndrome via Akt activation. *EMBO Mol. Med.* **16**, 132–157 (2024).
14. Oller, J. et al. Nitric oxide mediates aortic disease in mice deficient in the metalloprotease Adamts1 and in a mouse model of Marfan syndrome. *Nat. Med.* **23**, 200–212 (2017).
15. de la Fuente-Alonso, A. et al. Aortic disease in Marfan syndrome is caused by overactivation of sGC-PRKG signaling by NO. *Nat. Commun.* **12**, 2628 (2021).
16. Humphrey, J. D., Milewicz, D. M., Tellides, G. & Schwartz, M. A. Cell biology. Dysfunctional mechanosensing in aneurysms. *Science* **344**, 477–479 (2014).
17. Karimi, A. & Milewicz, D. M. Structure of the elastin-contractile units in the thoracic aorta and how genes that cause thoracic aortic aneurysms and dissections disrupt this structure. *Can. J. Cardiol.* **32**, 26–34 (2016).
18. Jensen, S. A., Robertson, I. B. & Handford, P. A. Dissecting the fibrillin microfibril: structural insights into organization and function. *Structure* **20**, 215–225 (2012).
19. Fruh, S. M., Schoen, I., Ries, J. & Vogel, V. Molecular architecture of native fibronectin fibrils. *Nat. Commun.* **6**, 7275 (2015).
20. Singh, P., Carraher, C. & Schwarzbauer, J. E. Assembly of fibronectin extracellular matrix. *Annu. Rev. Cell Dev. Biol.* **26**, 397–419 (2010).
21. Ensenberger, M. G. et al. Specific interactions between F1 adhesin of Streptococcus pyogenes and N-terminal modules of fibronectin. *J. Biol. Chem.* **276**, 35606–35613 (2001).
22. Tomasini-Johansson, B. R. et al. A 49-residue peptide from adhesin F1 of Streptococcus pyogenes inhibits fibronectin matrix assembly. *J. Biol. Chem.* **276**, 23430–23439 (2001).
23. Kadler, K. E., Hill, A. & Canty-Laird, E. G. Collagen fibrillogenesis: fibronectin, integrins, and minor collagens as organizers and nucleators. *Curr. Opin. Cell Biol.* **20**, 495–501 (2008).
24. Sabatier, L. et al. Fibrillin assembly requires fibronectin. *Mol. Biol. Cell* **20**, 846–858 (2009).
25. Humphrey, J. D., Dufresne, E. R. & Schwartz, M. A. Mechanotransduction and extracellular matrix homeostasis. *Nat. Rev. Mol. Cell Biol.* **15**, 802–812 (2014).
26. Lindeman, J. H. et al. Distinct defects in collagen microarchitecture underlie vessel-wall failure in advanced abdominal aneurysms and aneurysms in Marfan syndrome. *Proc. Natl. Acad. Sci. USA* **107**, 862–865 (2010).
27. Okamura, Y. et al. The extra domain A of fibronectin activates Toll-like receptor 4. *J. Biol. Chem.* **276**, 10229–10233 (2001).
28. Plow, E. F., Haas, T. A., Zhang, L., Loftus, J. & Smith, J. W. Ligand binding to integrins. *J. Biol. Chem.* **275**, 21785–21788 (2000).
29. Sanderson, R. D. & Bernfield, M. Molecular polymorphism of a cell surface proteoglycan: distinct structures on simple and stratified epithelia. *Proc. Natl. Acad. Sci. USA* **85**, 9562–9566 (1988).
30. Verfaillie, C. M., Benis, A., Iida, J., McGlave, P. B. & McCarthy, J. B. Adhesion of committed human hematopoietic progenitors to synthetic peptides from the C-terminal heparin-binding domain of fibronectin: cooperation between the integrin alpha 4 beta 1 and the CD44 adhesion receptor. *Blood* **84**, 1802–1811 (1994).
31. Chen, M. et al. FN (Fibronectin)-integrin α5 signaling promotes thoracic aortic aneurysm in a mouse model of marfan syndrome. *Arterioscler Thromb. Vasc. Biol.* **43**, e132–e150 (2023).
32. Fogerty, F. J., Akiyama, S. K., Yamada, K. M. & Mosher, D. F. Inhibition of binding of fibronectin to matrix assembly sites by anti-integrin (alpha 5 beta 1) antibodies. *J. Cell Biol.* **111**, 699–708 (1990).
33. Mao, Y. & Schwarzbauer, J. E. Fibronectin fibrillogenesis, a cell-mediated matrix assembly process. *Matrix Biol.* **24**, 389–399 (2005).
34. Nakamura, K. et al. Lineage-specific induced pluripotent stem cell-derived smooth muscle cell modeling predicts integrin alpha-V antagonism reduces aortic root aneurysm formation in Marfan syndrome mice. *Arterioscler. Thromb. Vasc. Biol.* **43**, 1134–1153 (2023).
35. Slack, R. J., Macdonald, S. J. F., Roper, J. A., Jenkins, R. G. & Hatley, R. J. D. Emerging therapeutic opportunities for integrin inhibitors. *Nat. Rev. Drug Discov.* **21**, 60–78 (2022).
36. Kim, H. et al. Irisin mediates effects on bone and fat via αV integrin receptors. *Cell* **175**, 1756–1768.e1717 (2018).
37. Curry, T., Barrameda, M. E., Thomas, T. C. & Esfandiarei, M. In vivo phenotypic vascular dysfunction extends beyond the aorta in a mouse model for fibrillin-1 (Fbn1) mutation. *Sci. Rep.* **14**, 5779 (2024).
38. Romaniello, F. et al. Aortopathy in Marfan syndrome: an update. *Cardiovasc. Pathol.* **23**, 261–266 (2014).
39. Cheng, B. et al. Nanoscale integrin cluster dynamics controls cellular mechanosensing via FAKY397 phosphorylation. *Sci. Adv.* **6**, eaax1909 (2020).
40. Persad, S. et al. Regulation of protein kinase B/Akt-serine 473 phosphorylation by integrin-linked kinase: critical roles for kinase activity and amino acids arginine 211 and serine 343. *J. Biol. Chem.* **276**, 27462–27469 (2001).
41. Alessi, D. R. et al. Characterization of a 3-phosphoinositide-dependent protein kinase which phosphorylates and activates protein kinase Balpha. *Curr. Biol.* **7**, 261–269 (1997).
42. Delcommenne, M. et al. Phosphoinositide-3-OH kinase-dependent regulation of glycogen synthase kinase 3 and protein kinase B/AKT by the integrin-linked kinase. *Proc. Natl. Acad. Sci. USA* **95**, 11211–11216 (1998).
43. Alfranca, A., Campanero, M. R. & Redondo, J. M. New methods for disease modeling using lentiviral vectors. *Trends Mol. Med.* **24**, 825–837 (2018).
44. Esteban, V. et al. Regulator of calcineurin 1 mediates pathological vascular wall remodeling. *J. Exp. Med.* **208**, 2125–2139 (2011).
45. Serrano, I. et al. Ilk conditional deletion in adult animals increases cyclic GMP-dependent vasorelaxation. *Cardiovasc. Res.* **99**, 535–544 (2013).
46. Wirth, A. et al. G12-G13-LARG-mediated signaling in vascular smooth muscle is required for salt-induced hypertension. *Nat. Med.* **14**, 64–68 (2008).
47. Borges, L. F. et al. Fibrinolytic activity is associated with presence of cystic medial degeneration in aneurysms of the ascending aorta. *Histopathology* **57**, 917–932 (2010).
48. Parker, S. J. et al. Proteomics reveals Rictor as a noncanonical TGF-beta signaling target during aneurysm progression in Marfan mice. *Am. J. Physiol. Heart Circ. Physiol.* **315**, H1112–H1126 (2018).

49. Zheng, P. S. et al. Versican/PG-M G3 domain promotes tumor growth and angiogenesis. *FASEB J.* **18**, 754–756 (2004).
50. Worth, D. C. et al. Alpha v beta3 integrin spatially regulates VASP and RIAM to control adhesion dynamics and migration. *J. Cell Biol.* **189**, 369–383 (2010).
51. Su, S. A. et al. Integrin alphaV emerges as a potential therapeutic target with cautionary implications in thoracic aortic aneurysm and dissection. *J. Thorac. Cardiovasc. Surg.* **171**, 886–895 (2025).
52. Buja, L. M., Zhao, B., Vela, D., Segura, A. & Narula, N. Pathobiology of aortic aneurysms and dissections: synthesis of recent investigations and evolving insights. *JACC Adv.* **4**, 101682 (2025).
53. Tan, C., Mui, A. & Dedhar, S. Integrin-linked kinase regulates inducible nitric oxide synthase and cyclooxygenase-2 expression in an NF-kappa B-dependent manner. *J. Biol. Chem.* **277**, 3109–3116 (2002).
54. Tsou, H. K. et al. Integrin-linked kinase is involved in TNF-alpha-induced inducible nitric-oxide synthase expression in myoblasts. *J. Cell Biochem.* **109**, 1244–1253 (2010).
55. Kogata, N., Tribe, R. M., Fässler, R., Way, M. & Adams, R. H. Integrin-linked kinase controls vascular wall formation by negatively regulating Rho/ROCK-mediated vascular smooth muscle cell contraction. *Genes Dev.* **23**, 2278–2283 (2009).
56. Fernández-Pisonero, I. et al. A hotspot mutation targeting the R-RAS2 GTPase acts as a potent oncogenic driver in a wide spectrum of tumors. *Cell Rep.* **38**, 110522 (2022).
57. Jiang, Q. et al. S6K1-mediated phosphorylation of PDK1 impairs AKT kinase activity and oncogenic functions. *Nat. Commun.* **13**, 1548 (2022).
58. Lynch, D. K., Ellis, C. A., Edwards, P. A. & Hiles, I. D. Integrin-linked kinase regulates phosphorylation of serine 473 of protein kinase B by an indirect mechanism. *Oncogene* **18**, 8024–8032 (1999).
59. Velling, T., Nilsson, S., Stefansson, A. & Johansson, S. beta1-Integrins induce phosphorylation of Akt on serine 473 independently of focal adhesion kinase and Src family kinases. *EMBO Rep.* **5**, 901–905 (2004).
60. Górska, A. & Mazur, A. J. Integrin-linked kinase (ILK): the known vs. the unknown and perspectives. *Cell Mol. Life Sci.* **79**, 100 (2022).
61. Sakai, T. et al. Integrin-linked kinase (ILK) is required for polarizing the epiblast, cell adhesion, and controlling actin accumulation. *Genes Dev.* **17**, 926–940 (2003).
62. Arnold, T. D., Zang, K. & Vallejo-Illarramendi, A. Deletion of integrin-linked kinase from neural crest cells in mice results in aortic aneurysms and embryonic lethality. *Dis. Model Mech.* **6**, 1205–1212 (2013).
63. Shen, D. et al. Aortic aneurysm generation in mice with targeted deletion of integrin-linked kinase in vascular smooth muscle cells. *Circ. Res.* **109**, 616–628 (2011).
64. Herranz, B. et al. Integrin-linked kinase regulates vasomotor function by preventing endothelial nitric oxide synthase uncoupling: role in atherosclerosis. *Circ. Res.* **110**, 439–449 (2012).
65. Judge, D. P. et al. Evidence for a critical contribution of haploinsufficiency in the complex pathogenesis of Marfan syndrome. *J. Clin. Investig.* **114**, 172–181 (2004).
66. Pontier, S. M. et al. Integrin-linked kinase has a critical role in ErbB2 mammary tumor progression: implications for human breast cancer. *Oncogene* **29**, 3374–3385 (2010).
67. Villahoz, S. et al. Conditional deletion of Rcan1 predisposes to hypertension-mediated intramural hematoma and subsequent aneurysm and aortic rupture. *Nat. Commun.* **9**, 4795 (2018).
68. Fischer, R. S., Myers, K. A., Gardel, M. L. & Waterman, C. M. Stiffness-controlled three-dimensional extracellular matrices for high-resolution imaging of cell behavior. *Nat. Protoc.* **7**, 2056–2066 (2012).
69. Huerta-Lopez, C. et al. Cell response to extracellular matrix viscous energy dissipation outweighs high-rigidity sensing. *Sci. Adv.* **10**, eadf9758 (2024).
70. Butt, H.-J. & Jaschke, M. Calculation of thermal noise in atomic force microscopy. *Nanotechnology* **6**, 1–7 (1995).
71. Wisniewski, J. R., Zougman, A., Nagaraj, N. & Mann, M. Universal sample preparation method for proteome analysis. *Nat. Methods* **6**, 359–362 (2009).
72. Wright, J. C. & Choudhary, J. S. DecoyPyrat: fast non-redundant hybrid decoy sequence generation for large scale proteomics. *J. Proteom. Bioinform.* **9**, 176–180 (2016).
73. Navarro, P. & Vazquez, J. A refined method to calculate false discovery rates for peptide identification using decoy databases. *J. Proteome Res* **8**, 1792–1796 (2009).
74. Bonzon-Kulichenko, E., Garcia-Marques, F., Trevisan-Herraz, M. & Vazquez, J. Revisiting peptide identification by high-accuracy mass spectrometry: problems associated with the use of narrow mass precursor windows. *J. Proteome Res.* **14**, 700–710 (2015).
75. Martinez-Bartolome, S. et al. Properties of average score distributions of SEQUEST: the probability ratio method. *Mol. Cell Proteom.* **7**, 1135–1145 (2008).
76. Navarro, P. et al. General statistical framework for quantitative proteomics by stable isotope labeling. *J. Proteome Res.* **13**, 1234–1247 (2014).
77. Garcia-Marques, F. et al. A novel systems-biology algorithm for the analysis of coordinated protein responses using quantitative proteomics. *Mol. Cell Proteom.* **15**, 1740–1760 (2016).
78. Rodriguez, J. M. et al. iSanXoT: a standalone application for the integrative analysis of mass spectrometry-based quantitative proteomics data. *Comput. Struct. Biotechnol. J.* **23**, 452–459 (2024).
79. Trevisan-Herraz, M. et al. SanXoT: a modular and versatile package for the quantitative analysis of high-throughput proteomics experiments. *Bioinformatics* **35**, 1594–1596 (2019).
80. Perez-Riverol, Y. et al. The PRIDE database at 20 years: 2025 update. *Nucleic Acids Res.* **53**, D543–D553 (2025).

Acknowledgements

We thank Dr. Sanjay Sinha for providing *Fbn1*$^{mgR/+}$ mice; Dr. Francisco Sánchez-Madrid for critically reading the manuscript; Verónica Labrador and Elvira Arza for technical support; Dr. Emilio Camafeita for support with mass spectrometry; and the CNIC facilities of microscopy, histology, flow cytometry, and advanced imaging. We want to particularly acknowledge the patients and the Hospital Universitari Vall d'Hebron Biobank (PT20/00107) integrated in the Platform ISCIII Biobanks and Biomodels for their collaboration and the Spanish Asociación de Afectados por el Sindrome de Marfan (SIMA) for their support. The CNIC is supported by the Instituto de Salud Carlos III (ISCIII), the Ministerio de Ciencia, Innovación y Universidades (MICIU) and the Pro CNIC Foundation, the CBM receives institutional support from Consejo Superior de Investigaciones Científicas, Universidad Autónoma de Madrid, and Fundación Ramón Areces. CBM and CNIC are recipients of "Severo Ochoa Excellence" grants (CEX2021-001154-S and CEX2020-001041-S, respectively) funded by MICIU/AEI/10.13039/501100011033. The project leading to these results has received funding from "La Caixa" Banking Foundation under project codes HR18-00068 (to M.R.C. and J.M.R.) and LCF/PR/HR22/52420019 (to J.V.); Spanish Ministerio de Ciencia e Innovación (MICIN) grant RTI2018-099246-B-I00 (MICIN/AEI/FEDER, UE) to J.M.R.; Spanish MICIU grants PID2020-115217RB-I00 (M.R.C.), PID2021-122388OB-I00 (J.M.R.), PID2021-122348NB-I00 (J.V.), PID2023-152367OB-I00 (M.R.C.), PID2023-147683NB-I00 (J.A.-C.), and PID2024-158276OB-100 (J.M.R.), funded by MICIU/AEI/10.13039/501100011033; Instituto de Salud Carlos III CIBER-CV CB16/11/00264 (J.M.R. and M.R.C.), CB16/11/00277 (J.V.), CB16/11/00303 (J.D.), CB16/11/00479 (G.T.T.), and CB16/00399 (J.A.-C.); and grants PI17/00381 to A.E. and PI21/00084 (co-funded by Fondo Europeo de Desarrollo Regional (FEDER) to J.F.N.); Fundacio La Marato TV3 (20151330 and 202334-31 to J.M.R.); "European Union NextGenerationEU/PRTR", S2022/BMD-7333-CM (INMUNOVAR-CM) to J.V., funded by Comunidad de Madrid; "ERDF A

way of making Europe", PLEC2022-009298, PLEC2022-009235 and EQC2021-007053-P to J.V., funded by MICIU/AEI/10.13039/501100011033; Redes Tematicas RED2024-154025-T to J.F.N., M.R.C., and J.M.R., and RED2022-134242-T to J.A.-C., funded by MICIU/AEI/10.13039/501100011033; Regional Government of Madrid grant Tec-NanoBio TEC-2024/TEC-158, (Bases Reguladoras 2402/2024; Convocatoria 3177/2024) to J.A.-C.; Spanish Ministerio de Ciencia e Innovación contracts FPI BES-2016-077649 (M.J.R.-R.), PRE2019-087460 (S.M.-G.), and PRE2022-104642 (N.M.-B.); Sara Borrell (CD18/00028) and Juan de la Cierva (IJC2020-044581-I) to M.T.; and FPU (20/04814) to I.A.-R.; and Regional Government of Madrid predoctoral contract (PIPF-2023SAL-GL-31131) to A.C.-M.

Author contributions

J.M.R. and M.R.C. conceived the study. I.A.-R., M.J.R.-R., M.T., S.M.-M., J.M.R., and M.R.C. designed the study and analyzed the data. I.A.-R., M.J.R.-R., S.M.-M., and M.T. performed most of the experiments, with contributions from N.M.-B., S.M.-G., T.G.-R., M.J.M.-O., D.L.-M., C.G.-M., C.C., and A.H.-A. J.V. supervised proteomics and bioinformatics analysis. E.H.G. and A.C.-M. performed stiffness studies under the supervision of J.A.-C. A.G., A.E., G.T.-T., and J.F.N. provided human tissue samples. D.R.-P. provided *Ilk*$^{f/f}$ mice. A.G., A.E., G.T.-T., J.F.N., D.R.-P., and J.D. provided ideas for the project. I.A.-R., J.M.R., and M.R.C. wrote the manuscript with contributions from S.M.-M., J.V., and J.A.-C. All authors read and approved the manuscript.

Competing interests

The authors declare no competing interests.

Additional information

Supplementary information The online version contains supplementary material available at https://doi.org/10.1038/s41467-026-74707-4.

Correspondence and requests for materials should be addressed to Juan Miguel Redondo or Miguel R. Campanero.

Peer review information *Nature Communications* thanks Mitra Esfandiarei, Bhama Ramkhelawon, and the other, anonymous, reviewer(s) for their contribution to the peer review of this work. A peer review file is available.

[1]Gene regulation in cardiovascular remodeling and inflammation group, Centro Nacional de Investigaciones Cardiovasculares (CNIC), Madrid, Spain. [2]Centro de Investigación Biomédica en Red de Enfermedades Cardiovasculares (CIBERCV), Madrid, Spain. [3]Tissue & Organ Homeostasis Program, Centro de Biologia Molecular Severo Ochoa (CBM), Consejo Superior de Investigaciones Científicas-Universidad Autónoma de Madrid, Madrid, Spain. [4]Molecular Mechanics of the Cardiovascular System, CNIC, Madrid, Spain. [5]Department of Cardiology, Hospital Universitari Vall d'Hebron & Vall d'Hebron Institut de Recerca (VHIR), Barcelona, Spain. [6]Teknon Medical Centre-Quironsalud, Heart Institute, Barcelona, Spain. [7]Department of Medicine, Universidad de Alcalá de Henares & Nephrology Department, Hospital Príncipe de Asturias, Alcalá de Henares; Instituto Ramon y Cajal de Investigación Sanitaria (IRYCIS), Fundación Renal Iñigo Álvarez de Toledo (FRIAT) & RICOR from Instituto de Salud Carlos III and NOVELREN from Comunidad de Madrid, Madrid, Spain. [8]Cardiovascular Surgery, Hospital Universitario Marqués de Valdecilla, Instituto de Investigación Valdecilla (IDIVAL), Facultad de Medicina, Universidad de Cantabria, Santander, Spain. [9]Cardiovascular Proteomics, CNIC, Madrid, Spain. [10]Department of Pharmacology, School of Pharmacy, University of Granada, Granada, Spain. [11]Present address: Department of Surgery (Cardiac), Yale School of Medicine, New Haven, CT, USA. [12]Present address: Department of Pharmacology, School of Pharmacy, University of Granada, Granada, Spain. [13]Present address: Microscopy and Dynamic Imaging Unit, CNIC, Madrid, Spain. [14]These authors contributed equally: María Jesús Ruiz-Rodríguez, Sara Martínez-Martínez, Marta Toral. [15]These authors jointly supervised this work: Juan Miguel Redondo, Miguel R. Campanero. ✉e-mail: jmredondo@cbm.csic.es; mcampanero@cbm.csic.es